


A Reduced-Order Electrochemical Model of Li-Ion Batteries for Control and Estimation Applications

Guodong Fan , Xiaoyu Li, and Marcello Canova

Abstract—In this paper, a reduced-order electrochemical model of lithium-ion batteries is developed for control and estimation applications through analytical model order reduction based on a Galerkin projection method. The governing diffusion partial differential equations in the liquid and solid phases are approximated into low-order systems of ordinary differential equations while the physical meaning of all model parameters is preserved, allowing one to perform state and parameter estimation. The selection of basis functions for the Galerkin projection method and model order truncation is carefully determined based on analysis both in the frequency and time domains. With the reduced-order diffusion models in the liquid and solid phases, an extended single particle model incorporating the electrolyte dynamics is developed. The model is then validated against the experimental data gathered from two batteries with different chemistries (lithium nickel manganese cobalt oxide/graphite and lithium iron phosphate oxide/graphite) at different input conditions. Results show that the reduced-order model agrees very well with experimental data at various conditions. Meanwhile, it can be simulated thousands of times faster than the real time, making it suitable for long-term-life simulation, control, and estimation applications.

Index Terms—Extended single particle model, lithium ion batteries, model order selection, reduced-order model.

I. INTRODUCTION

LITHIUM ion batteries are considered the state of the art for energy storage in electric and hybrid vehicles. However, there are still several major challenges, such as battery safety, durability and cost, limiting the widespread application of Li-ion batteries in electrified vehicles [1]–[5]. Understanding and predicting the chemical and physical processes in Li-ion cells leading to the above issues is possible through multi-scale characterization methods. However, “in-situ” quantification of such processes is usually not achievable due to the absence of direct measurements. In this regard, the estimation of battery State of Charge (SOC) and State of Health (SOH) is essential to monitor the available energy and ensure safe operations. Several control-oriented models have been developed to predict

SOC and SOH in automotive energy storage systems [6]–[13]. While these models have a simple and intuitive structure, they do not capture the physical processes related to the transport of lithium in the solid and liquid phase, which are the foundation to an accurate description of the performance and degradation in Li-ion cells. Hence, high-fidelity, first-principles models are an essential investigation tool for the prediction of the battery performance and life. Furthermore, such models provide a mean to monitor and control the charging and discharging process of battery cells and packs, in relation with usage and environmental factors and in presence of limited sensing [14]–[18].

Electrochemical battery models based on first principles, such as the pseudo two-dimensional model (or the P2D model) [19] and Single Particle Model (SPM) [20], have been widely used to understand the underlying physical and chemical processes occurring in the batteries and predict the concentration dynamics and terminal voltage. Recently, Extended Single Particle Model (ESPM) [21], [22], incorporating the electrolyte dynamics, has gained significant popularity for fast simulation, control estimation applications due to its simple model structure and high accuracy in predicting battery cell behaviors even at high C-rates conditions.

While the ESPM is able to accurately predict the cell terminal voltage as function of current and temperature, it is still considerably complex from a mathematical standpoint, as it is based upon sets of coupled linear or nonlinear PDEs and nonlinear algebraic equations. Numerical methods such as Finite Element Method (FEM) and Finite Difference Method (FDM) have been applied to approximate the PDEs by discretizing the space domain [23]. However, to accurately predict the spatially-distributed variables of the original PDE systems, a large number of discretization nodes (and, ultimately, of equations) is required, leading to significant computational challenges when applied to fast simulation and to estimation or control design.

For the above reasons, considerable research efforts have been devoted to apply Model Order Reduction (MOR) techniques to first-principle models of lithium ion batteries, including polynomial approximation [24], Padé approximation [25], residue grouping [26], Balanced Truncation (BT) [27] and Proper Orthogonal Decomposition (POD) [28]. The objective of applying MOR techniques is to approximate the governing PDEs into low-order systems of ODEs that can be solved with standard simulation tools. In recent times, the Galerkin projection method has also been applied to analytically approximate the diffusion PDEs in electrochemical models [29]–[31]. The main advantage of this method is that it is able to provide

Manuscript received March 8, 2017; revised May 30, 2017 and July 13, 2017; accepted August 3, 2017. Date of publication August 11, 2017; date of current version January 15, 2018. This work was supported by the National Science Foundation under Award CMMI-1554063. The review of this paper was coordinated by the Guest Editors of the VPPC 2016 Special Section. (Corresponding author: Guodong Fan.)

G. Fan and M. Canova are with the Center for Automotive Research, The Ohio State University, Columbus, OH 43212 USA (e-mail: fan.267@osu.edu; canova.1@osu.edu).

X. Li is with the School of Electrical Engineering and Automation, Harbin Institute of Technology, Harbin 150001, China (e-mail: xiaoyu070220202@126.com).

Digital Object Identifier 10.1109/TVT.2017.2738780

accurate predictions of the concentration profile in the whole cell domain while retain the physical meaning of all model parameters. This is especially important for SOC/SOH estimation and cycle life prediction, since the analytical form of the Reduced-Order Models (ROM) allows one to perform state and parameter estimation. In addition, the accuracy of the Galerkin projection method is comparable to numerical MOR methods such as POD and BT, at a fraction of the computational cost [27]. However, the solid/electrolyte interface boundary conditions in the liquid diffusion PDE are neglected by the above research, because it is not trivial to define trial functions for the composite domains (i.e. cathode/separator/anode) and the amount of symbolic manipulations becomes extremely challenging, particularly the selection of basis functions and trial solution for each sub-domain, the calculation of the analytical solution of the inner products, and the reformulation of the system by considering the algebraic constraints applied at the interfaces. In [32], a nonlinear diffusion model is developed to predict the behavior of a lithium ion battery cell particularly for low temperature and high current conditions. However, it is not suitable for real-time control and estimation applications due to significant computational complexity. In addition, the impact of different choices of basis functions used in the Galerkin projection method and model order truncation on the model accuracy, which is another contribution of this work, has not been addressed yet.

In this paper, we extend the aforementioned research by developing a ROM for lithium ion batteries through a systemic application of the Galerkin projection method. This paper also extends our previous work [31] by approximating the liquid diffusion PDE into a linear low-order ODE system and by investigating the impact of the choice of the basis functions as well as the order truncation on model accuracy.

The paper is structured as follows. The following section introduces the complete ESPM. Next, a ROM is developed by reducing the governing diffusion PDEs in the ESPM to low-order ODE system by systematically using the Galerkin projection method. The choice of basis functions and truncation order is determined by investigating the trade-off between the model order and the ROM's ability to capture the dynamics in the frequency and time domains. Finally, the ROM is extensively validated against the experimental data gathered from two batteries with different chemistries at different input conditions.

II. OVERVIEW OF THE EXTENDED SINGLE PARTICLE MODEL

A schematic of an electrochemical lithium ion cell model is shown in Fig. 1. The cell model consists of three domains, namely the positive electrode, the separator and the negative electrode. The model describes the physical processes that occur during cell operations. During charging, lithium ions deintercalate from the active material particles in positive electrode and are deposited into the electrolyte solution. Then the ions are transported within the liquid region by diffusion and ionic conduction, through the separator, to the surface of active material particles in negative electrode where they intercalate and store within the active material.

The ESPM approximates the pseudo two-dimensional model based on the Porous Electrode Theory on a microscopic scale

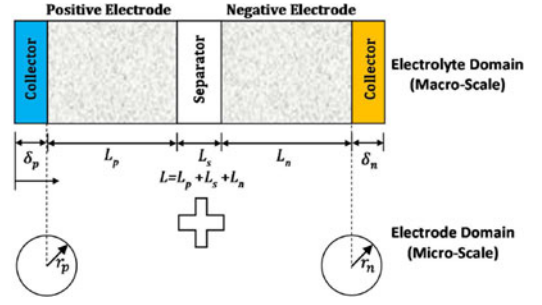


Fig. 1. Schematic of the ESPM battery model.

with a set of decoupled PDEs [19]. The model assumes that each electrode can be represented by a single spherical particle, and the total surface area of the particle is equivalent to the overall area of the active material in the porous electrode, as shown in Fig. 1. In addition, the intercalation current density is assumed to be uniform throughout the thickness of each electrode [20], [33]. It is worth noting that, unlike the conventional Single Particle Model (SPM), where the electrolyte overpotential in the liquid phase is approximated as quasi-static, the electrolyte dynamics are included in the ESPM to capture the cell behavior under high C-rates conditions [21], [22], [32].

The intercalation/deintercalation process is modeled according to the Fick's law over a spherical domain, which describes the diffusion of lithium concentration in an active material particle:

$$\frac{\partial c_{s,k}(r,t)}{\partial t} = D_{s,k} \frac{\partial^2 c_{s,k}(r,t)}{\partial r^2} + \frac{2D_{s,k}}{r} \frac{\partial c_{s,k}(r,t)}{\partial r} \quad (1)$$

with boundary conditions:

$$\begin{aligned} \left. \frac{\partial c_{s,k}(r,t)}{\partial r} \right|_{r=0} &= 0 \\ D_{s,k} \left. \frac{\partial c_{s,k}(r,t)}{\partial r} \right|_{r=R_k} &= -\frac{J_k(t)}{F} \end{aligned} \quad (2)$$

where the subscript $k = p$ for the positive electrode and $k = n$ for the negative electrode, $c_{s,k}$ denotes the lithium concentration in the solid phase, $D_{s,k}$ is the diffusion coefficient, $a_k = 3\varepsilon_k/R_k$ represents the surface area per unit volume, ε_k is the electrode active volume fraction, and R_k is the active particle radius, F is the Faraday constant and J_k is the intercalation current density, which acts as the input to the dynamics of the diffusion. For the ESPM, J_k is assumed to be uniform in each electrode, and can be expressed as:

$$J_k(t) = \begin{cases} \frac{I(t)}{a_k AL_k} & , k = p \\ -\frac{I(t)}{a_k AL_k} & , k = n \end{cases} \quad (3)$$

where $I(t)$ is the applied current, A denotes total area of the current collector, L_p and L_n indicate the thickness of the positive electrode, and the negative electrode respectively, as shown in Fig. 1.

The lithium concentration in the liquid phase is governed by:

$$\varepsilon_{e,k} \frac{\partial c_e(x,t)}{\partial t} = D_{e,k} \frac{\partial^2 c_e(x,t)}{\partial x^2} + a_k \frac{1-t_0^+}{F} J_k(t) \quad (4)$$

with zero flux conditions at the boundaries:

$$\begin{aligned} \left. \frac{\partial c_e(x, t)}{\partial x} \right|_{x=0} &= 0 \\ \left. \frac{\partial c_e(x, t)}{\partial x} \right|_{x=L} &= 0 \end{aligned} \quad (5)$$

where c_e is the lithium concentration in the liquid phase, t_0^+ represents the transference number, and $D_{e,k}$ is the effective diffusion coefficient. Empirical observations have been shown that transport is slower than predicted [34], and therefore the reported diffusion coefficient is usually combined with an assumed Bruggeman coefficient and an experimentally tuned porosity value to compute the effective diffusion coefficient [19]:

$$D_e = D\varepsilon^{\text{brugg}} \quad (6)$$

where D is the diffusion coefficient and $\varepsilon^{\text{brugg}}$ is the Bruggeman coefficient, which is used to modify the diffusion coefficient based on the tortuosity of the conduction or diffusion path.

Additional boundary conditions should also be posed to satisfy the continuity of the concentration and flux at the solid/liquid interface, since $\varepsilon_{e,k}$, $D_{e,k}$ and J_k have different values in the positive electrode, the separator and the negative electrode:

$$\begin{aligned} c_e(x, t)|_{x=L_p^-} &= c_e(x, t)|_{x=L_p^+} \\ c_e(x, t)|_{x=L_p+L_s^-} &= c_e(x, t)|_{x=L_p+L_s^+} \\ -D_{e,p} \left. \frac{\partial c_e(x, t)}{\partial x} \right|_{x=L_p^-} &= -D_{e,s} \left. \frac{\partial c_e(x, t)}{\partial x} \right|_{x=L_p^+} \\ -D_{e,s} \left. \frac{\partial c_e(x, t)}{\partial x} \right|_{x=L_p+L_s^-} &= -D_{e,n} \left. \frac{\partial c_e(x, t)}{\partial x} \right|_{x=L_p+L_s^+} \end{aligned} \quad (7)$$

where L_s is the thickness of the separator.

The concentration in solid and liquid phase are then coupled by the kinetic overpotential η_k , given by the Butler-Volmer equation [19]:

$$\begin{aligned} J_k(t) &= i_{0,k}(t) \left[\exp\left(\frac{\alpha n_e F}{\bar{R}T} \eta_k(t)\right) \right. \\ &\quad \left. - \exp\left(-\frac{(1-\alpha) n_e F}{\bar{R}T} \eta_k(t)\right) \right] \end{aligned} \quad (8)$$

where \bar{R} is the gas constant, T is the temperature, α is the transfer coefficient, n_e is the number of electrons that are lost or gained during the chemical reaction, and $i_{0,k}$ denotes the exchange current density, which is defined as:

$$i_{0,k}(t) = F K_k \sqrt{c_{s,surf,k}(c_{s,max,k} - c_{s,surf,k})c_{e,0}} \quad (9)$$

where K_k is the kinetic rate constant, $c_{s,max,k}$ is the saturation concentration of the electrode, $c_{s,surf,k}$ is the electrode surface concentration, and $c_{e,0}$ is the average concentration.

Normally, the symmetry factor α is assumed as 0.5 [19], and $n_e = 1$ since one electron is released per atom of lithium de-intercalating. Then, the kinetic overpotential η_k can be expressed as:

$$\eta_k(t) = \frac{\bar{R}T}{\alpha F} \sinh^{-1} \left(\frac{J_k(t)}{2i_{0,k}(t)} \right) \quad (10)$$

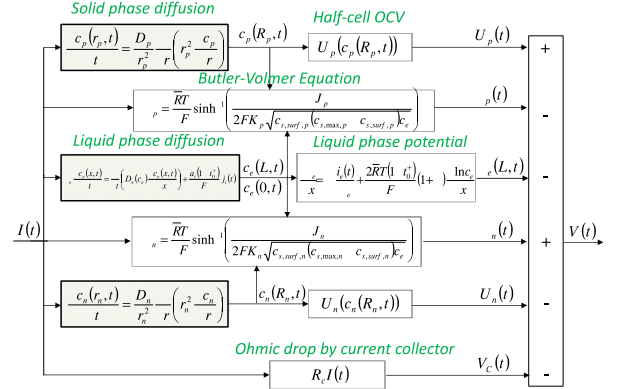


Fig. 2. Block diagram of the ESPM for a Li-ion cell.

The potential in the liquid phase ϕ_e is related to the liquid concentration in the following way:

$$\frac{\partial}{\partial x} \left(\kappa^{eff} \frac{\partial \phi_e(x, t)}{\partial x} \right) + \frac{\partial}{\partial x} \left(\kappa_D^{eff} \frac{\partial \ln c_e(x, t)}{\partial x} \right) + J_k(t) = 0 \quad (11)$$

The integration of (11) over x yields:

$$\frac{\partial \phi_e(x, t)}{\partial x} = -\frac{i_e(t)}{\kappa^{eff}} + \frac{\kappa_D^{eff}}{\kappa^{eff}} \frac{\partial \ln c_e(x, t)}{\partial x} \quad (12)$$

where i_e is the ionic current in the electrolyte, κ^{eff} is the effective ionic conductivity and κ_D^{eff} is defined as the effective diffusional conductivity [19]:

$$\kappa_D^{eff} = \frac{2\bar{R}T\kappa^{eff}(1-t_0^+)}{F}(1+\beta) \quad (13)$$

where β is the activity coefficient and is assumed to be constant in this work.

The block diagram of the cell model is shown in Fig. 2, from which the cell output voltage can be obtained as:

$$\begin{aligned} V_{cell}(t) &= \phi_s(0, t) - \phi_s(L, t) - IR_c \\ &= (U_p(c_{s,surf,p}, t) - U_n(c_{s,surf,n}, t)) \\ &\quad - (\eta_p(0, t) - \eta_n(L, t)) \\ &\quad - (\phi_e(0, t) - \phi_e(L, t)) - IR_c \end{aligned} \quad (14)$$

where the Open-Circuit Potentials (OCPs) U_k ($k = p, n$) are determined as a function of the surface concentrations in the solid phase, and R_c represents Ohmic resistance of the current collectors. The OCP curves for the positive and negative electrodes are normally obtained from half-cell experiments at thermodynamic equilibrium conditions.

III. MODEL ORDER REDUCTION OF THE ESPM USING GALERKIN PROJECTION METHOD

The Galerkin projection method is applied to approximate the concentration profiles in (1) and (4) in the ESPM via projection on a reduced basis.

In the case of diffusion in the liquid phase, the continuity boundary conditions of the concentration and flux at the solid/liquid interfaces significantly increase the complexity of using the method directly. Attempts at applying this method to reduce the diffusion PDE in the electrolyte solution have

been recently made by simplifying or neglecting these interface boundary conditions [29]–[31]. However, by considering the interface boundary conditions, prediction of the lithium concentration profile cross the cell (ultimately, the cell terminal voltage) would be much different than the case when the interface boundary conditions are absent. Therefore, without incorporating the interface boundary conditions, accuracy loss may be anticipated in the resulting ROMs, especially at low-temperature, high C-rate conditions and for large-format batteries, where large concentration gradients are more common to see. As mentioned previously, the difficulties of incorporating the interface boundary conditions are the definition of trial functions for the composite domains and the significant amount of symbolic manipulations in the pre-processing phase.

In the case of the solid phase diffusion, further complications arise due to the presence of the non-zero, time-varying boundary conditions that express the ionic flux at the electrode surface.

In this section, the application of the Galerkin projection method to the diffusion PDEs in the electrochemical model will be discussed in detail, and the challenges mentioned above will be addressed.

A. Model Order Reduction of Liquid Phase Diffusion PDEs

As mentioned previously, the difficulties of incorporating the interface boundary conditions are the definition of trial functions for the composite domains and the significant amount of symbolic manipulations in the pre-processing phase. The parabolic PDE describing the Li^+ concentration in the liquid phase is recalled here for convenience:

$$\varepsilon_{e,k} \frac{\partial c_e(x,t)}{\partial t} = D_{e,k} \frac{\partial^2 c_e(x,t)}{\partial x^2} + a_k \frac{1-t_0^+}{F} J_k(t) \quad (15)$$

with the boundary conditions:

$$\left. \frac{\partial c_e(x,t)}{\partial x} \right|_{x=0} = 0 \quad (16)$$

$$\left. \frac{\partial c_e(x,t)}{\partial x} \right|_{x=L} = 0 \quad (17)$$

$$c_e(x,t)|_{x=L_p^-} = c_e(x,t)|_{x=L_p^+} \quad (18)$$

$$c_e(x,t)|_{x=L_p+L_s^-} = c_e(x,t)|_{x=L_p+L_s^+} \quad (19)$$

$$-D_{e,p} \left. \frac{\partial c_e(x,t)}{\partial x} \right|_{x=L_p^-} = -D_{e,s} \left. \frac{\partial c_e(x,t)}{\partial x} \right|_{x=L_p^+} \quad (20)$$

$$-D_{e,s} \left. \frac{\partial c_e(x,t)}{\partial x} \right|_{x=L_p+L_s^-} = -D_{e,n} \left. \frac{\partial c_e(x,t)}{\partial x} \right|_{x=L_p+L_s^+} \quad (21)$$

For simplicity, a dimensionless length is introduced to define each region:

$$\begin{aligned} x_p &= \frac{x}{L_p}, \quad 0 \leq x < L_p \\ x_s &= \frac{x-L_p}{L_s}, \quad L_p \leq x < L_p + L_s \\ x_n &= \frac{x-L_p-L_s}{L_n}, \quad L_p + L_s \leq x \leq L \end{aligned} \quad (22)$$

It can be shown in (16) that the concentration flux in the liquid phase is not continuous at the liquid/solid interfaces, since $D_{e,k}$ usually takes different values in different regions. In this case, trial solutions for $c_e(x,t)$ are selected separately for each region:

$$\begin{aligned} \hat{c}_{e,p}(x_p,t) &= c_e(x_p,0) + \sum_{i=1}^N p_i(t) \psi_i(x_p) \\ \hat{c}_{e,s}(x_s,t) &= c_e(x_s,0) + \sum_{i=1}^N s_i(t) \psi_i(x_s) \\ \hat{c}_{e,n}(x_n,t) &= c_e(x_n,0) + \sum_{i=1}^N n_i(t) \psi_i(x_n) \end{aligned} \quad (23)$$

where $c_e(x_p,0)$, $c_e(x_s,0)$ and $c_e(x_n,0)$ are the initial concentration at the three regions, $\psi_i(x_k)$ are basis functions, $p_i(t)$, $s_i(t)$ and $n_i(t)$ are the time-varying coefficients of the basis functions for each region, and N is the number of the basis functions. Commonly used basis functions are listed in Table I, and include the Legendre polynomials, Chebyshev polynomials of the first kind, Chebyshev polynomials of the second kind, and the sinusoidal functions [35], [36]. The number and mathematical expression of the basis functions, which affects the order of the resulting ROM, is generally determined heuristically, namely by evaluating the trade-off between accuracy and mathematical complexity for different orders of truncation. More details will be presented later in Section III-C. For the time being, we assume that three shifted and normalized Legendre polynomials in (24) are sufficient to approximate the lithium concentration in the electrolyte solution.

$$\begin{aligned} \psi_1(x_k) &= 1 \\ \psi_2(x_k) &= \sqrt{3}(2x_k - 1) \\ \psi_3(x_k) &= \frac{\sqrt{5}}{2} [3(2x_k - 1)^2 - 1] \end{aligned} \quad (24)$$

The diffusion PDE and boundary conditions can be written using dimensionless coordinates as:

$$\varepsilon_{e,k} \frac{\partial c_{e,k}(x_k,t)}{\partial t} = \frac{D_{e,k}}{L_k^2} \frac{\partial^2 c_{e,k}(x_k,t)}{\partial x_k^2} + a_k \frac{1-t_0^+}{F} J_k(t) \quad (25)$$

$$\left. \frac{\partial c_{e,p}(x_p,t)}{\partial x_p} \right|_{x_p=0} = 0$$

$$\left. \frac{\partial c_{e,n}(x_n,t)}{\partial x_n} \right|_{x_n=1} = 0$$

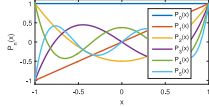
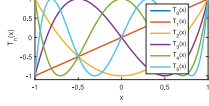
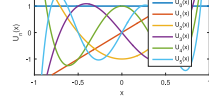
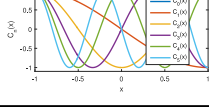
$$c_{e,p}(x_p,t)|_{x_p=1} = c_{e,s}(x_s,t)|_{x_s=0}$$

$$c_{e,s}(x_s,t)|_{x_s=1} = c_{e,n}(x_n,t)|_{x_n=0}$$

$$\begin{aligned} \frac{\varepsilon_{e,p}^{\text{bruggp}}}{L_p} \left. \frac{\partial c_{e,p}(x_p,t)}{\partial x_p} \right|_{x_p=1} &= \frac{\varepsilon_{e,s}^{\text{bruggs}}}{L_s} \left. \frac{\partial c_{e,s}(x_s,t)}{\partial x_s} \right|_{x_s=0} \\ \frac{\varepsilon_{e,s}^{\text{bruggs}}}{L_s} \left. \frac{\partial c_{e,s}(x_s,t)}{\partial x_s} \right|_{x_s=1} &= \frac{\varepsilon_{e,n}^{\text{bruggn}}}{L_n} \left. \frac{\partial c_{e,n}(x_n,t)}{\partial x_n} \right|_{x_n=0} \end{aligned} \quad (26)$$

The last two equations result from the continuity of concentration at the solid/liquid interfaces and the effective diffusion coefficient $D_{e,k}$ in (6).

TABLE I
SUMMARY OF COMMONLY USED BASIS FUNCTIONS

	General expression	Graphic illustration
Legendre Polynomials (LP)	$P_n(x) = 2^n \cdot \sum_{k=0}^n x^k \binom{n}{k} \binom{n+k-1}{n}$	
Chebyshev Polynomials of the 1st Kind (ChP1)	$T_n(x) = n \sum_{k=0}^n (-2)^k \frac{(n+k-1)!}{(n-k)!(2k)!} (1-x)^k$	
Chebyshev Polynomials of the 2nd Kind (ChP2)	$U_n(x) = \sum_{k=0}^n (-2)^k \frac{(n+k-1)!}{(n-k)!(2k+1)!} (1-x)^k$	
Cosine Functions (Cos)	$C_n(x) = \cos\left(\frac{n\pi(x+1)}{2}\right)$	

The residuals are obtained by substituting the trial solution (23) into (25):

$$R_{c_{e,k}}(x_k, t) = \varepsilon_{e,k} \frac{\partial \hat{c}_{e,k}(x_k, t)}{\partial t} - \frac{D_{e,k}}{L_k^2} \frac{\partial^2 \hat{c}_{e,k}(x_k, t)}{\partial x_k^2} - a_k \frac{1-t_0^+}{F} J_k(x_k, t) \quad (27)$$

or

$$R_{c_{e,k}}(x_k, t) = \varepsilon_{e,k} \sum_{i=1}^N \dot{k}_i(t) \psi_i(x_k) - \frac{D_{e,k}}{L_k^2} \sum_{i=1}^N k_i(t) \psi_i''(x_k) - a_k \frac{1-t_0^+}{F} J_k(x_k, t) \quad (28)$$

where $k_i(t)$ is used to represent the coefficients $p_i(t)$, $s_i(t)$ and $n_i(t)$.

In addition, it should be noted that the choice of basis functions should satisfy the boundary conditions in (26). Substitution of (23) and the first three Legendre polynomials in (24) into (26) yields six algebraic equations with respect to the time-varying coefficients $p_i(t)$, $s_i(t)$ and $n_i(t)$:

$$\begin{aligned} \sqrt{3}p_2(t) - 3\sqrt{5}p_3(t) &= 0 \\ \sqrt{3}n_2(t) - 3\sqrt{5}n_3(t) &= 0 \\ p_1(t) + \sqrt{3}p_2(t) + \sqrt{5}p_3(t) - s_1(t) + \sqrt{3}s_2(t) - \sqrt{5}s_3(t) &= 0 \\ s_1(t) + \sqrt{3}s_2(t) + \sqrt{5}s_3(t) - n_1(t) + \sqrt{3}n_2(t) - \sqrt{5}n_3(t) &= 0 \\ \frac{\varepsilon_{e,p}^{\text{brugg}_p}}{L_p} \left(\sqrt{3}p_2(t) + 3\sqrt{5}p_3(t) \right) & \\ - \frac{\varepsilon_{e,s}^{\text{brugg}_s}}{L_s} \left(\sqrt{3}s_2(t) + 3\sqrt{5}s_3(t) \right) &= 0 \\ \frac{\varepsilon_{e,s}^{\text{brugg}_s}}{L_s} \left(\sqrt{3}s_2(t) + 3\sqrt{5}s_3(t) \right) & \\ - \frac{\varepsilon_{e,n}^{\text{brugg}_n}}{L_n} \left(\sqrt{3}n_2(t) + 3\sqrt{5}n_3(t) \right) &= 0 \end{aligned} \quad (29)$$

Then, the Galerkin projection method is applied to minimize the residuals in (28) by making the inner products of the residuals and each basis function be zeros. Nine ODEs with respect to the time-varying coefficients $p_i(t)$, $s_i(t)$ and $n_i(t)$ are obtained as a result:

$$\begin{aligned} \int_0^1 \psi_1(x_p) R_{c_{e,p}}(x_p, t) dx_p &= 0 \\ \text{Positive Electrode: } \int_0^1 \psi_2(x_p) R_{c_{e,p}}(x_p, t) dx_p &= 0 \\ \int_0^1 \psi_3(x_p) R_{c_{e,p}}(x_p, t) dx_p &= 0 \\ \int_0^1 \psi_1(x_s) R_{c_{e,s}}(x_s, t) dx_s &= 0 \\ \text{Separator: } \int_0^1 \psi_2(x_s) R_{c_{e,s}}(x_s, t) dx_s &= 0 \\ \int_0^1 \psi_3(x_s) R_{c_{e,s}}(x_s, t) dx_s &= 0 \\ \int_0^1 \psi_1(x_n) R_{c_{e,n}}(x_n, t) dx_n &= 0 \\ \text{Negative Electrode: } \int_0^1 \psi_2(x_n) R_{c_{e,n}}(x_n, t) dx_n &= 0 \\ \int_0^1 \psi_3(x_n) R_{c_{e,n}}(x_n, t) dx_n &= 0 \end{aligned} \quad (30)$$

Equation (30) can be rewritten in matrix form:

$$\begin{bmatrix} \dot{p}_1 \\ \dot{p}_2 \\ \dot{p}_3 \\ \dot{s}_1 \\ \dot{s}_2 \\ \dot{s}_3 \\ \dot{n}_1 \\ \dot{n}_2 \\ \dot{n}_3 \end{bmatrix} = \begin{bmatrix} a_{p,1}^{\psi_1} & a_{p,2}^{\psi_1} & a_{p,3}^{\psi_1} & 0 & 0 & 0 & 0 & 0 & 0 \\ a_{p,1}^{\psi_2} & a_{p,2}^{\psi_2} & a_{p,3}^{\psi_2} & 0 & 0 & 0 & 0 & 0 & 0 \\ a_{p,1}^{\psi_3} & a_{p,2}^{\psi_3} & a_{p,3}^{\psi_3} & 0 & 0 & 0 & 0 & 0 & 0 \\ 0 & 0 & 0 & a_{s,1}^{\psi_1} & a_{s,2}^{\psi_1} & a_{s,3}^{\psi_1} & 0 & 0 & 0 \\ 0 & 0 & 0 & a_{s,1}^{\psi_2} & a_{s,2}^{\psi_2} & a_{s,3}^{\psi_2} & 0 & 0 & 0 \\ 0 & 0 & 0 & a_{s,1}^{\psi_3} & a_{s,2}^{\psi_3} & a_{s,3}^{\psi_3} & 0 & 0 & 0 \\ 0 & 0 & 0 & 0 & 0 & 0 & a_{n,1}^{\psi_1} & a_{n,2}^{\psi_1} & a_{n,3}^{\psi_1} \\ 0 & 0 & 0 & 0 & 0 & 0 & a_{n,1}^{\psi_2} & a_{n,2}^{\psi_2} & a_{n,3}^{\psi_2} \\ 0 & 0 & 0 & 0 & 0 & 0 & a_{n,1}^{\psi_3} & a_{n,2}^{\psi_3} & a_{n,3}^{\psi_3} \end{bmatrix} \begin{bmatrix} p_1 \\ p_2 \\ p_3 \\ s_1 \\ s_2 \\ s_3 \\ n_1 \\ n_2 \\ n_3 \end{bmatrix} + \begin{bmatrix} b_{p,1} \\ b_{p,2} \\ b_{p,3} \\ b_{s,1} \\ b_{s,2} \\ b_{s,3} \\ b_{n,1} \\ b_{n,2} \\ b_{n,3} \end{bmatrix} I \quad (31)$$

where

$$a_{k,i}^{\psi_1} = \frac{D_{e,k}}{L_k^2} \int_0^1 \psi_1(x_k) \psi_i''(x_k) dx_k$$

$$\varepsilon_{e,k} \int_0^1 \psi_1(x_k) \psi_1(x_k) dx_k$$

$$a_{k,i}^{\psi_2} = \frac{D_{e,k}}{L_k^2} \int_0^1 \psi_2(x_k) \psi_i''(x_k) dx_k$$

$$\varepsilon_{e,k} \int_0^1 \psi_2(x_k) \psi_2(x_k) dx_k$$

$$a_{k,i}^{\psi_3} = \frac{D_{e,k}}{L_k^2} \int_0^1 \psi_3(x_k) \psi_i''(x_k) dx_k$$

$$\varepsilon_{e,k} \int_0^1 \psi_3(x_k) \psi_3(x_k) dx_k$$

$$b_{k,i} = \frac{1-t_0^+}{F} \frac{1}{a_k AL_k} J_k \int_0^1 \psi_i(x_k) dx_k$$

$$\varepsilon_{e,k} \int_0^1 \psi_i(x_k) \psi_i(x_k) dx_k$$

It can be noticed that the system is over-determined, since it includes nine ODEs in (31) and six algebraic constraints in (29), while only nine variables need to be solved. Considering that the six boundary conditions represented by (29) must be satisfied at any time, the three remaining equations can be obtained by choosing $p_1(t)$, $s_1(t)$ and $n_1(t)$ as independent variables. Thus, the size of the differentiation matrix in (31) is reduced by one row and one column for each boundary condition considered,

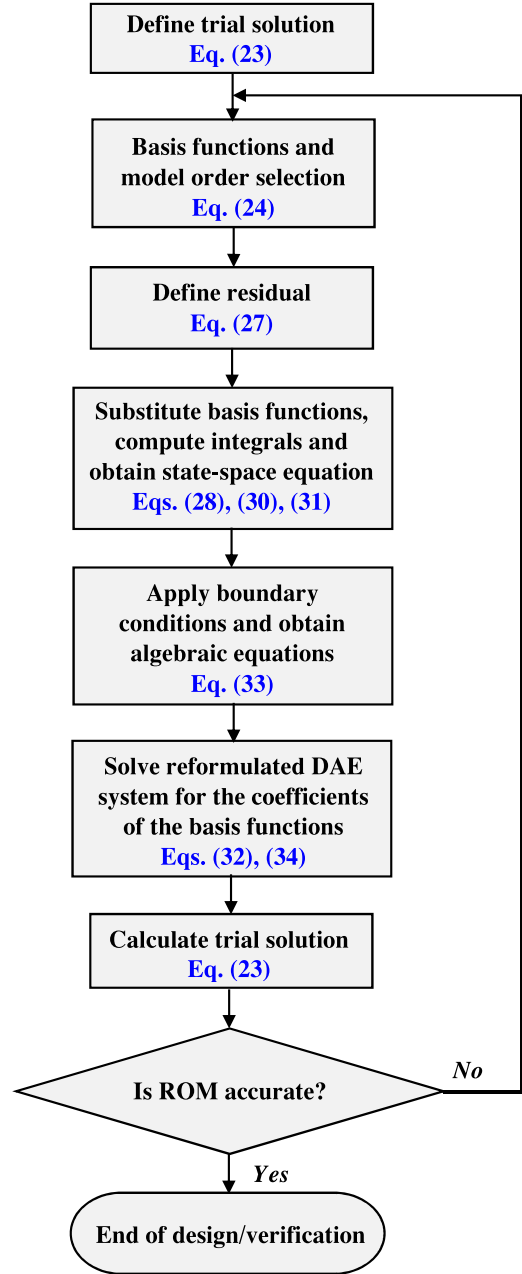


Fig. 3. Flow chart of the application of the Galerkin projection method.

leading to a reduced differentiation matrix that automatically satisfies the boundary conditions.

The system is now reformulated as eq. (32) shown at the next page, where Θ is the algebraic function obtained by (29), which expresses the dependent variables in terms of $p_1(t)$, $s_1(t)$ and $n_1(t)$. The expression of Θ can be found in (33) as shown at the next to next page.

Once $p_1(t)$, $s_1(t)$, $n_1(t)$ are solved by (32), the other six coefficients can be calculated using (34) as shown at the next to next page, which is derived from (29). Finally, the electrolyte concentration in each region can be obtained using (23). The complete procedure of the Galerkin projection method can be found in the flow chart in Fig. 3, where the procedure is briefly described, and the equations used in the procedure are listed as well.

It is worth mentioning that although the amount of symbolic manipulation in (30)–(33) is very challenging, all coefficients in (32), namely $a_{k,i}^{\psi_j}$, $b_{k,j}$ and Θ , can be obtained analytically in the preprocessing phase. No further computational effort is needed to calculate these coefficients during simulation, which guarantees the simulation efficiency of the ROM. More details on the simulation time will be reported in Section IV.

B. Model Order Reduction of Solid Phase Diffusion PDEs

For the solid phase diffusion, no interface boundary conditions are posed. However, extension of this methodology to the solid phase is complicated by the presence of the non-zero, time-dependent boundary conditions. Therefore, an approach based on coordinate transformation is adopted here to obtain a reduced order model [31].

$$\begin{bmatrix} \dot{p}_1 \\ \dot{s}_1 \\ \dot{n}_1 \end{bmatrix} = \begin{bmatrix} a_{p,1}^{\psi_1} + a_{p,2}^{\psi_1} \Theta_{p_2 \rightarrow p_1} + a_{p,3}^{\psi_1} \Theta_{p_3 \rightarrow p_1} & a_{p,2}^{\psi_1} \Theta_{p_2 \rightarrow s_1} + a_{p,3}^{\psi_1} \Theta_{p_3 \rightarrow s_1} & a_{p,2}^{\psi_1} \Theta_{p_2 \rightarrow n_1} + a_{p,3}^{\psi_1} \Theta_{p_3 \rightarrow n_1} \\ a_{s,2}^{\psi_1} \Theta_{s_2 \rightarrow p_1} + a_{s,3}^{\psi_1} \Theta_{s_3 \rightarrow p_1} & a_{s,1}^{\psi_1} + a_{s,2}^{\psi_1} \Theta_{s_2 \rightarrow s_1} + a_{s,3}^{\psi_1} \Theta_{s_3 \rightarrow s_1} & a_{s,2}^{\psi_1} \Theta_{s_2 \rightarrow n_1} + a_{s,3}^{\psi_1} \Theta_{s_3 \rightarrow n_1} \\ a_{n,2}^{\psi_1} \Theta_{n_2 \rightarrow p_1} + a_{n,3}^{\psi_1} \Theta_{n_3 \rightarrow p_1} & a_{n,2}^{\psi_1} \Theta_{n_2 \rightarrow s_1} + a_{n,3}^{\psi_1} \Theta_{n_3 \rightarrow s_1} & a_{p,3}^{\psi_3} + a_{n,2}^{\psi_1} \Theta_{n_2 \rightarrow n_1} + a_{n,3}^{\psi_1} \Theta_{n_3 \rightarrow n_1} \end{bmatrix} \begin{bmatrix} p_1 \\ s_1 \\ n_1 \end{bmatrix} + \begin{bmatrix} b_{p,1} \\ b_{s,1} \\ b_{n,1} \end{bmatrix} I \quad (32)$$

$$\begin{aligned} \Theta_{p_2 \rightarrow p_1} &= -\frac{\sqrt{3}}{2} \cdot \frac{2L_n L_p \varepsilon_s^{2\text{brugg}_s} + 2L_p L_s \varepsilon_s^{\text{brugg}_s} \varepsilon_n^{\text{brugg}_n}}{4L_n L_p \varepsilon_s^{2\text{brugg}_s} + 4L_n L_s \varepsilon_p^{\text{brugg}_p} \varepsilon_s^{\text{brugg}_s} + 4L_p L_s \varepsilon_n^{\text{brugg}_n} \varepsilon_s^{\text{brugg}_s} + 3L_s^2 \varepsilon_p^{\text{brugg}_p} \varepsilon_n^{\text{brugg}_n}} \\ \Theta_{p_2 \rightarrow s_1} &= \frac{\sqrt{3}}{2} \cdot \frac{2L_n L_p \varepsilon_s^{2\text{brugg}_s} + 3L_p L_s \varepsilon_s^{\text{brugg}_s} \varepsilon_n^{\text{brugg}_n}}{4L_n L_p \varepsilon_s^{2\text{brugg}_s} + 4L_n L_s \varepsilon_p^{\text{brugg}_p} \varepsilon_s^{\text{brugg}_s} + 4L_p L_s \varepsilon_n^{\text{brugg}_n} \varepsilon_s^{\text{brugg}_s} + 3L_s^2 \varepsilon_p^{\text{brugg}_p} \varepsilon_n^{\text{brugg}_n}} \\ \Theta_{p_2 \rightarrow n_1} &= -\frac{\sqrt{3}}{2} \cdot \frac{L_p L_s \varepsilon_s^{\text{brugg}_s} \varepsilon_n^{\text{brugg}_n}}{4L_n L_p \varepsilon_s^{2\text{brugg}_s} + 4L_n L_s \varepsilon_p^{\text{brugg}_p} \varepsilon_s^{\text{brugg}_s} + 4L_p L_s \varepsilon_n^{\text{brugg}_n} \varepsilon_s^{\text{brugg}_s} + 3L_s^2 \varepsilon_p^{\text{brugg}_p} \varepsilon_n^{\text{brugg}_n}} \\ \Theta_{p_3 \rightarrow p_1} &= -\frac{\sqrt{5}}{10} \cdot \frac{2L_n L_p \varepsilon_s^{2\text{brugg}_s} + 2L_p L_s \varepsilon_s^{\text{brugg}_s} \varepsilon_n^{\text{brugg}_n}}{4L_n L_p \varepsilon_s^{2\text{brugg}_s} + 4L_n L_s \varepsilon_p^{\text{brugg}_p} \varepsilon_s^{\text{brugg}_s} + 4L_p L_s \varepsilon_n^{\text{brugg}_n} \varepsilon_s^{\text{brugg}_s} + 3L_s^2 \varepsilon_p^{\text{brugg}_p} \varepsilon_n^{\text{brugg}_n}} \\ \Theta_{p_3 \rightarrow s_1} &= \frac{\sqrt{5}}{10} \cdot \frac{2L_n L_p \varepsilon_s^{2\text{brugg}_s} + 3L_p L_s \varepsilon_s^{\text{brugg}_s} \varepsilon_n^{\text{brugg}_n}}{4L_n L_p \varepsilon_s^{2\text{brugg}_s} + 4L_n L_s \varepsilon_p^{\text{brugg}_p} \varepsilon_s^{\text{brugg}_s} + 4L_p L_s \varepsilon_n^{\text{brugg}_n} \varepsilon_s^{\text{brugg}_s} + 3L_s^2 \varepsilon_p^{\text{brugg}_p} \varepsilon_n^{\text{brugg}_n}} \\ \Theta_{p_3 \rightarrow p_1} &= -\frac{\sqrt{5}}{10} \cdot \frac{L_p L_s \varepsilon_s^{\text{brugg}_s} \varepsilon_n^{\text{brugg}_n}}{4L_n L_p \varepsilon_s^{2\text{brugg}_s} + 4L_n L_s \varepsilon_p^{\text{brugg}_p} \varepsilon_s^{\text{brugg}_s} + 4L_p L_s \varepsilon_n^{\text{brugg}_n} \varepsilon_s^{\text{brugg}_s} + 3L_s^2 \varepsilon_p^{\text{brugg}_p} \varepsilon_n^{\text{brugg}_n}} \\ \Theta_{s_2 \rightarrow p_1} &= -\frac{\sqrt{3}L_s}{2} \cdot \frac{2L_n \varepsilon_p^{\text{brugg}_p} \varepsilon_s^{\text{brugg}_s} + L_s \varepsilon_p^{\text{brugg}_p} \varepsilon_n^{\text{brugg}_n}}{4L_n L_p \varepsilon_s^{2\text{brugg}_s} + 4L_n L_s \varepsilon_p^{\text{brugg}_p} \varepsilon_s^{\text{brugg}_s} + 4L_p L_s \varepsilon_n^{\text{brugg}_n} \varepsilon_s^{\text{brugg}_s} + 3L_s^2 \varepsilon_p^{\text{brugg}_p} \varepsilon_n^{\text{brugg}_n}} \\ \Theta_{s_2 \rightarrow s_1} &= -\frac{\sqrt{3}L_s}{2} \cdot \frac{2L_n \varepsilon_p^{\text{brugg}_p} \varepsilon_s^{\text{brugg}_s} - 2L_p \varepsilon_s^{\text{brugg}_s} \varepsilon_n^{\text{brugg}_n}}{4L_n L_p \varepsilon_s^{2\text{brugg}_s} + 4L_n L_s \varepsilon_p^{\text{brugg}_p} \varepsilon_s^{\text{brugg}_s} + 4L_p L_s \varepsilon_n^{\text{brugg}_n} \varepsilon_s^{\text{brugg}_s} + 3L_s^2 \varepsilon_p^{\text{brugg}_p} \varepsilon_n^{\text{brugg}_n}} \\ \Theta_{s_2 \rightarrow n_1} &= \frac{\sqrt{3}L_s}{2} \cdot \frac{2L_p \varepsilon_s^{2\text{brugg}_s} \varepsilon_n^{\text{brugg}_n} + L_s \varepsilon_p^{\text{brugg}_p} \varepsilon_n^{\text{brugg}_n}}{4L_n L_p \varepsilon_s^{2\text{brugg}_s} + 4L_n L_s \varepsilon_p^{\text{brugg}_p} \varepsilon_s^{\text{brugg}_s} + 4L_p L_s \varepsilon_n^{\text{brugg}_n} \varepsilon_s^{\text{brugg}_s} + 3L_s^2 \varepsilon_p^{\text{brugg}_p} \varepsilon_n^{\text{brugg}_n}} \\ \Theta_{s_3 \rightarrow p_1} &= -\frac{\sqrt{5}L_s}{10} \cdot \frac{2L_n \varepsilon_p^{\text{brugg}_p} \varepsilon_s^{\text{brugg}_s} + 3L_s \varepsilon_p^{\text{brugg}_p} \varepsilon_n^{\text{brugg}_n}}{4L_n L_p \varepsilon_s^{2\text{brugg}_s} + 4L_n L_s \varepsilon_p^{\text{brugg}_p} \varepsilon_s^{\text{brugg}_s} + 4L_p L_s \varepsilon_n^{\text{brugg}_n} \varepsilon_s^{\text{brugg}_s} + 3L_s^2 \varepsilon_p^{\text{brugg}_p} \varepsilon_n^{\text{brugg}_n}} \\ \Theta_{s_3 \rightarrow s_1} &= \frac{\sqrt{5}L_s}{10} \cdot \frac{2L_n \varepsilon_p^{\text{brugg}_p} \varepsilon_s^{\text{brugg}_s} + 2L_p \varepsilon_s^{\text{brugg}_s} \varepsilon_n^{\text{brugg}_n}}{4L_n L_p \varepsilon_s^{2\text{brugg}_s} + 4L_n L_s \varepsilon_p^{\text{brugg}_p} \varepsilon_s^{\text{brugg}_s} + 4L_p L_s \varepsilon_n^{\text{brugg}_n} \varepsilon_s^{\text{brugg}_s} + 3L_s^2 \varepsilon_p^{\text{brugg}_p} \varepsilon_n^{\text{brugg}_n}} \\ \Theta_{s_3 \rightarrow n_1} &= -\frac{\sqrt{5}L_s}{10} \cdot \frac{2L_p \varepsilon_s^{2\text{brugg}_s} \varepsilon_n^{\text{brugg}_n} + 3L_s \varepsilon_p^{\text{brugg}_p} \varepsilon_n^{\text{brugg}_n}}{4L_n L_p \varepsilon_s^{2\text{brugg}_s} + 4L_n L_s \varepsilon_p^{\text{brugg}_p} \varepsilon_s^{\text{brugg}_s} + 4L_p L_s \varepsilon_n^{\text{brugg}_n} \varepsilon_s^{\text{brugg}_s} + 3L_s^2 \varepsilon_p^{\text{brugg}_p} \varepsilon_n^{\text{brugg}_n}} \end{aligned}$$

$$\begin{aligned}
\Theta_{n_2 \rightarrow p_1} &= -\frac{\sqrt{3}\varepsilon_s^{\text{brugg}_s} L_n}{2} \cdot \frac{L_s \varepsilon_p^{\text{brugg}_p}}{4L_n L_p \varepsilon_s^{2\text{brugg}_s} + 4L_n L_s \varepsilon_p^{\text{brugg}_p} \varepsilon_s^{\text{brugg}_s} + 4L_p L_s \varepsilon_n^{\text{brugg}_n} \varepsilon_s^{\text{brugg}_s} + 3L_s^2 \varepsilon_p^{\text{brugg}_p} \varepsilon_n^{\text{brugg}_n}} \\
\Theta_{n_2 \rightarrow s_1} &= \frac{\sqrt{3}\varepsilon_s^{\text{brugg}_s} L_n}{2} \cdot \frac{2L_p \varepsilon_s^{2\text{brugg}_s} + 3L_s \varepsilon_p^{\text{brugg}_p}}{4L_n L_p \varepsilon_s^{2\text{brugg}_s} + 4L_n L_s \varepsilon_p^{\text{brugg}_p} \varepsilon_s^{\text{brugg}_s} + 4L_p L_s \varepsilon_n^{\text{brugg}_n} \varepsilon_s^{\text{brugg}_s} + 3L_s^2 \varepsilon_p^{\text{brugg}_p} \varepsilon_n^{\text{brugg}_n}} \\
\Theta_{n_2 \rightarrow n_1} &= -\frac{\sqrt{3}\varepsilon_s^{\text{brugg}_s} L_n}{2} \cdot \frac{2L_p \varepsilon_s^{2\text{brugg}_s} + 2L_s \varepsilon_p^{\text{brugg}_p}}{4L_n L_p \varepsilon_s^{2\text{brugg}_s} + 4L_n L_s \varepsilon_p^{\text{brugg}_p} \varepsilon_s^{\text{brugg}_s} + 4L_p L_s \varepsilon_n^{\text{brugg}_n} \varepsilon_s^{\text{brugg}_s} + 3L_s^2 \varepsilon_p^{\text{brugg}_p} \varepsilon_n^{\text{brugg}_n}} \\
\Theta_{n_3 \rightarrow p_1} &= \frac{\sqrt{5}\varepsilon_s^{\text{brugg}_s} L_n}{10} \cdot \frac{L_s \varepsilon_p^{\text{brugg}_p}}{4L_n L_p \varepsilon_s^{2\text{brugg}_s} + 4L_n L_s \varepsilon_p^{\text{brugg}_p} \varepsilon_s^{\text{brugg}_s} + 4L_p L_s \varepsilon_n^{\text{brugg}_n} \varepsilon_s^{\text{brugg}_s} + 3L_s^2 \varepsilon_p^{\text{brugg}_p} \varepsilon_n^{\text{brugg}_n}} \\
\Theta_{n_3 \rightarrow s_1} &= -\frac{\sqrt{5}\varepsilon_s^{\text{brugg}_s} L_n}{10} \cdot \frac{2L_p \varepsilon_s^{2\text{brugg}_s} + 3L_s \varepsilon_p^{\text{brugg}_p}}{4L_n L_p \varepsilon_s^{2\text{brugg}_s} + 4L_n L_s \varepsilon_p^{\text{brugg}_p} \varepsilon_s^{\text{brugg}_s} + 4L_p L_s \varepsilon_n^{\text{brugg}_n} \varepsilon_s^{\text{brugg}_s} + 3L_s^2 \varepsilon_p^{\text{brugg}_p} \varepsilon_n^{\text{brugg}_n}} \\
\Theta_{n_3 \rightarrow n_1} &= \frac{\sqrt{5}\varepsilon_s^{\text{brugg}_s} L_n}{10} \cdot \frac{2L_p \varepsilon_s^{2\text{brugg}_s} + 2L_s \varepsilon_p^{\text{brugg}_p}}{4L_n L_p \varepsilon_s^{2\text{brugg}_s} + 4L_n L_s \varepsilon_p^{\text{brugg}_p} \varepsilon_s^{\text{brugg}_s} + 4L_p L_s \varepsilon_n^{\text{brugg}_n} \varepsilon_s^{\text{brugg}_s} + 3L_s^2 \varepsilon_p^{\text{brugg}_p} \varepsilon_n^{\text{brugg}_n}} \quad (33)
\end{aligned}$$

$$\begin{aligned}
p_2 &= -\frac{\sqrt{3}}{2} \cdot \frac{\left(2L_n L_p \varepsilon_s^{2\text{brugg}_s} + 2L_p L_s \varepsilon_s^{\text{brugg}_s} \varepsilon_n^{\text{brugg}_n}\right) p_1 - \left(2L_n L_p \varepsilon_s^{2\text{brugg}_s} + 3L_p L_s \varepsilon_s^{\text{brugg}_s} \varepsilon_n^{\text{brugg}_n}\right) s_1 + L_p L_s \varepsilon_s^{\text{brugg}_s} \varepsilon_n^{\text{brugg}_n} n_1}{4L_n L_p \varepsilon_s^{2\text{brugg}_s} + 4L_n L_s \varepsilon_p^{\text{brugg}_p} \varepsilon_s^{\text{brugg}_s} + 4L_p L_s \varepsilon_n^{\text{brugg}_n} \varepsilon_s^{\text{brugg}_s} + 3L_s^2 \varepsilon_p^{\text{brugg}_p} \varepsilon_n^{\text{brugg}_n}} \\
p_3 &= \frac{\sqrt{3}}{3\sqrt{5}} p_2 \\
s_2 &= -\frac{\sqrt{3}L_s}{2} \cdot \frac{\left(2L_n \varepsilon_p^{\text{brugg}_p} \varepsilon_s^{\text{brugg}_s} + L_s \varepsilon_p^{\text{brugg}_p} \varepsilon_n^{\text{brugg}_n}\right) p_1 - \left(2L_n \varepsilon_p^{2\text{brugg}_p} \varepsilon_s^{\text{brugg}_s} - 2L_p \varepsilon_s^{\text{brugg}_s} \varepsilon_n^{\text{brugg}_n}\right) s_1 - \left(2L_p \varepsilon_s^{2\text{brugg}_s} \varepsilon_n^{\text{brugg}_n} + L_s \varepsilon_p^{\text{brugg}_p} \varepsilon_n^{\text{brugg}_n}\right) n_1}{4L_n L_p \varepsilon_s^{2\text{brugg}_s} + 4L_n L_s \varepsilon_p^{\text{brugg}_p} \varepsilon_s^{\text{brugg}_s} + 4L_p L_s \varepsilon_n^{\text{brugg}_n} \varepsilon_s^{\text{brugg}_s} + 3L_s^2 \varepsilon_p^{\text{brugg}_p} \varepsilon_n^{\text{brugg}_n}} \\
s_3 &= -\frac{\sqrt{5}L_s}{10} \cdot \frac{\left(2L_n \varepsilon_p^{\text{brugg}_p} \varepsilon_s^{\text{brugg}_s} + 3L_s \varepsilon_p^{\text{brugg}_p} \varepsilon_n^{\text{brugg}_n}\right) p_1 - \left(2L_n \varepsilon_p^{2\text{brugg}_p} \varepsilon_s^{\text{brugg}_s} + 2L_p \varepsilon_s^{\text{brugg}_s} \varepsilon_n^{\text{brugg}_n}\right) s_1 + \left(2L_p \varepsilon_s^{2\text{brugg}_s} \varepsilon_n^{\text{brugg}_n} + 3L_s \varepsilon_p^{\text{brugg}_p} \varepsilon_n^{\text{brugg}_n}\right) n_1}{4L_n L_p \varepsilon_s^{2\text{brugg}_s} + 4L_n L_s \varepsilon_p^{\text{brugg}_p} \varepsilon_s^{\text{brugg}_s} + 4L_p L_s \varepsilon_n^{\text{brugg}_n} \varepsilon_s^{\text{brugg}_s} + 3L_s^2 \varepsilon_p^{\text{brugg}_p} \varepsilon_n^{\text{brugg}_n}} \quad (34) \\
n_2 &= -\frac{\sqrt{3}\varepsilon_s^{\text{brugg}_s} L_n}{2} \cdot \frac{L_s \varepsilon_p^{\text{brugg}_p} p_1 - \left(2L_p \varepsilon_s^{2\text{brugg}_s} + 3L_s \varepsilon_p^{\text{brugg}_p}\right) s_1 + \left(2L_p \varepsilon_s^{2\text{brugg}_s} + 2L_s \varepsilon_p^{\text{brugg}_p}\right) n_1}{4L_n L_p \varepsilon_s^{2\text{brugg}_s} + 4L_n L_s \varepsilon_p^{\text{brugg}_p} \varepsilon_s^{\text{brugg}_s} + 4L_p L_s \varepsilon_n^{\text{brugg}_n} \varepsilon_s^{\text{brugg}_s} + 3L_s^2 \varepsilon_p^{\text{brugg}_p} \varepsilon_n^{\text{brugg}_n}} \\
n_3 &= -\frac{\sqrt{3}}{3\sqrt{5}} n_2
\end{aligned}$$

For convenience, the boundary value problem describing the diffusion in solid phase is recalled. The subscript k is dropped for simplicity. The PDE describing the process is written as:

$$\frac{\partial c_s(r, t)}{\partial t} = D_s \frac{\partial^2 c_s(r, t)}{\partial r^2} + \frac{2D_s}{r} \frac{\partial c_s(r, t)}{\partial r} \quad (35)$$

with boundary conditions:

$$\begin{aligned}
\left. \frac{\partial c_s(r, t)}{\partial r} \right|_{r=0} &= 0 \\
D_s \left. \frac{\partial c_s(r, t)}{\partial r} \right|_{r=R} &= -\frac{J(t)}{F} \quad (36)
\end{aligned}$$

The difficulty of applying the Galerkin method to the solid phase diffusion lies in the time-varying boundary condition at $r = R$. Typical orthogonal basis functions, such as Legendre

polynomials and Chebyshev polynomials are all time independent, hence do not satisfy the boundary conditions automatically. However, this problem could be overcome by redefining a new variable as:

$$\Gamma(r, t) = c_s(r, t) + \frac{J(t)}{FD_s} \cdot \frac{r^2}{2R} \quad (37)$$

Substituting into (35) gives:

$$\begin{aligned}
\frac{\partial \Gamma(r, t)}{\partial t} &= D_s \frac{\partial^2 \Gamma(r, t)}{\partial r^2} + \frac{2D_s}{r} \frac{\partial \Gamma(r, t)}{\partial r} \\
&\quad - \frac{3}{FR} J(t) + \frac{r^2}{2RF D_s} \cdot \dot{J}(t) \quad (38)
\end{aligned}$$

with a new set of boundary conditions:

$$\begin{aligned} \left. \frac{\partial \Gamma(r, t)}{\partial r} \right|_{r=0} &= 0 \\ \left. \frac{\partial \Gamma(r, t)}{\partial r} \right|_{r=R} &= 0 \end{aligned} \quad (39)$$

The trial solution $\hat{\Gamma}(r, t)$ can be written as:

$$\hat{\Gamma}(r, t) = c_s(r, 0) + \sum_{i=0}^N w_i(t) \psi_i(r) \quad (40)$$

With this change of coordinates, the boundary conditions in (36) become time independent, which enables the implementation of several time-independent basis functions for the projection. In this case, the basis functions should have continuous first and second derivatives in their region of validity. More importantly, the trial solution, which is the linear combination of the basis functions, should satisfy the boundary conditions in (39). Otherwise, additional constraints must be imposed to the coefficients of the basis functions.

Substituting the trial solution into (38), the residual is obtained as:

$$\begin{aligned} R_{\Gamma}(r, t) &= \frac{\partial \hat{\Gamma}(r, t)}{\partial t} - D_s \frac{\partial^2 \hat{\Gamma}(r, t)}{\partial r^2} + \frac{2D_s}{r} \frac{\partial \hat{\Gamma}(r, t)}{\partial r} \\ &+ \frac{3}{FR} J(t) - \frac{r^2}{2RFD_s} \cdot \dot{J}(t) \end{aligned} \quad (41)$$

Applying the Galerkin projection method, a state space representation is obtained:

$$\dot{\mathbf{w}} = \mathbf{A}\mathbf{w} + \mathbf{B}_1 u + \mathbf{B}_2 \dot{u} \quad (42)$$

where

$$\begin{aligned} A_{i,j} &= \frac{D_s \int_0^R \psi_i(r) \psi_j''(r) + \frac{2D_s}{r} \psi_i(r) \psi_j'(r) dr}{\int_0^R \psi_i(r) \psi_i(r) dr} \\ B_{1,i} &= \frac{-\frac{3}{FR} \int_0^R \psi_i(r) \frac{1}{aAL} dr}{\int_0^R \psi_i(r) \psi_i(r) dr} \\ B_{2,i} &= \frac{\frac{1}{2RFD_s} \int_0^R \psi_i(r) r^2 \frac{1}{aAL} dr}{\int_0^R \psi_i(r) \psi_i(r) dr} \end{aligned} \quad (43)$$

$\mathbf{w} = [w_1, w_2, \dots, w_N]^T$, and $u(t)$ is the applied current $I(t)$.

Note that (42) is not in standard state space form, due to the presence of the time derivative of the input. This term can be eliminated by introducing a new coordinate:

$$\mathbf{z} = \mathbf{w} - \mathbf{B}_2 u \quad (44)$$

$$\dot{\mathbf{z}} = \mathbf{A}\mathbf{z} + (\mathbf{B}_1 + \mathbf{A}\mathbf{B}_2) u \triangleq \mathbf{A}\mathbf{z} + \mathbf{B}u \quad (45)$$

Once the time-varying coefficients $z_i(t)$ are solved, the lithium concentration in the solid phase can be obtained:

$$\begin{aligned} c_s(r, t) &= \Gamma(r, t) - \frac{J(t)}{FD_s} \cdot \frac{r^2}{2R} \\ &= c_s(r, 0) + \mathbf{\Psi}^T \mathbf{w} - \frac{J(t)}{FD_s} \cdot \frac{r^2}{2R} \\ &= c_s(r, 0) + \mathbf{C}\mathbf{z} + \mathbf{D}u \end{aligned} \quad (46)$$

where $\mathbf{\Psi} = [\psi_1(r); \dots; \psi_N(r)]$, and

$$\mathbf{C} = \mathbf{\Psi}^T$$

$$\mathbf{D} = \mathbf{\Psi}^T \mathbf{B}_2 - \frac{1}{aFD_s AL} \cdot \frac{r^2}{2R}$$

C. Assessment of Different Basis Functions and Orders of Truncation on Model Accuracy

Before the implementation of the resulting ROMs for simulations, the analytical expression of the basis functions and the order of the series (which affects the order of the ROMs) should be determined. To the best of the authors' knowledge, there is no available standard procedure of the selection of basis functions and model order yet for the Galerkin projection method, and we believe this contribution presents a significant innovation to the state of the art. In this section, the impact of different choices of basis functions and truncations of model order on the ROM accuracy will be evaluated. The analysis is done with reference to the response in the frequency and domains, with the goal of examining the influence of the order of truncation for each class of basis functions on the accuracy of the resulting ROMs.

1) *Frequency Domain Analysis*: One way to determine the appropriate order for a ROM is to compare the frequency responses of the ROMs with the PDE-based model. Thus, the truncation order can be decided by setting a trade-off between the model order and the ROM's ability to capture the frequency response of the PDE-based model. In this section, a single-input and single-output system (SISO) is obtained in this study where the frequency response of the electrode surface concentration is examined, since the surface concentration governs many respects of the cell behavior. Since (35) is a linear PDE in time, the Laplace transform method can be adopted to obtain a set of ODEs in the complex domain, which can be solved and inverse-transformed to obtain a transcendental transfer function [22], [25]. For instance, the transfer function linking the surface concentration within the electrode to the input current can be obtained by solving the boundary value problem in and (36), and is given by [22]:

$$\frac{C_s(R, s)}{J(s)} = \frac{R \sinh\left(\sqrt{\frac{s}{D_s}} R\right)}{D_s \left(\sqrt{\frac{s}{D_s}} R \cosh\left(\sqrt{\frac{s}{D_s}} R\right) - \sinh\left(\sqrt{\frac{s}{D_s}} R\right) \right)} \quad (47)$$

The frequency response diagrams of the SISO models obtained using different basis functions are presented in Fig. 4, up to the sixth order of truncation. The first order is skipped here because the frequency response of the first-order ROM is the same as that of the second-order ROM for all the polynomial

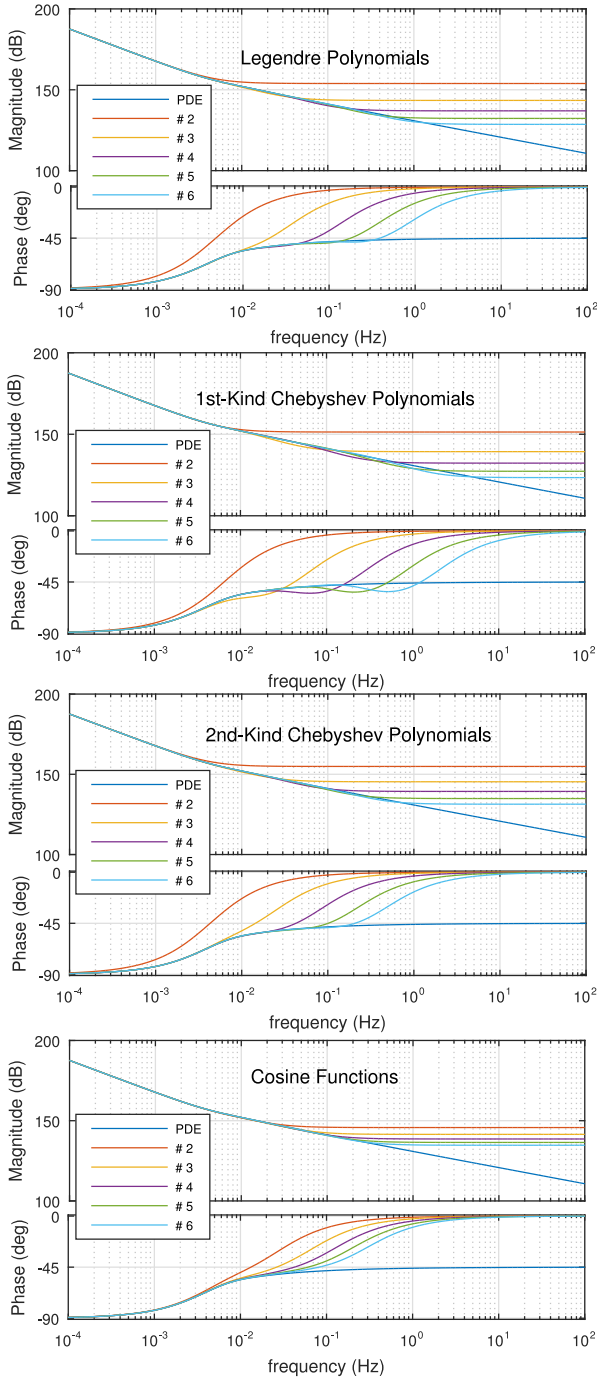


Fig. 4. Frequency response of electrode surface concentration for the Galerkin projection method using different basis functions and different model orders.

basis functions, and the coefficient $w_2(t)$ of the second basis function $\psi_2(r)$ is forced to be a constant zero to satisfy the boundary condition at $r = R$. However, it is worth mentioning that ROMs generated by the cosine basis functions do not have this problem, since no additional constraints are needed. The frequency response obtained by the ROMs is then compared against the one obtained from applying the Laplace transform to the original spherical diffusion PDE.

As expected, all the ROMs obtained with different basis functions capture well the steady-state response of the system, es-

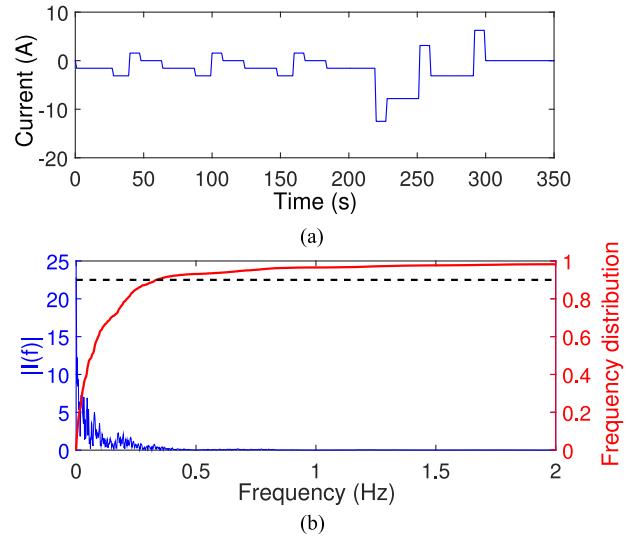


Fig. 5. USABC input current profile. (a) Input current. (b) Frequency distributions.

pecially in the low-frequency domain, and the accuracy range increases with the order of the ROM. However, it is shown in Fig. 4 that the high-frequency response of the ROMs is approximated as a static gain. This occurs because the coordinate transformation adopted to remove the time-dependent boundary condition introduces an input term in (37), resulting in a non-strictly proper transfer function that leads to a non-zero feedforward matrix D in the state space realization. Consequently, ROMs obtained by applying the Galerkin projection method lose in part the low-pass filtering characteristics of the original PDEs, and ultimately accuracy might degrade for high-frequency input signals.

Nonetheless, it has been shown in [22] that the frequency content of the battery current profile obtained from regulatory driving cycles, such as the US06 highway cycle, the Federal Urban Dynamometer Schedule (FUDS), and the United States Advanced Battery Consortium (USABC) PHEV dynamic charge depleting duty cycle, is largely distributed in the low-frequency domain (less than 2 Hz). For instance, 90% of the signal power of the USABC cycle profile is distributed within frequencies less than 0.4 Hz, as shown in Fig. 5. Therefore, it is possible to determine an optimal order of truncation for the solid diffusion ROM generated by each class of basis functions by examining the frequency response at a cut-off frequency of 0.4 Hz.

Fig. 6 shows the error on the magnitude of the frequency response obtained using different basis functions at different model orders. The error is obtained by comparing the magnitude of the frequency response of the original spherical diffusion PDE with those of the ROMs. The error threshold values are set as ± 3 dB for illustration purposes. In fact, the threshold values should be determined based on the desired accuracy of required for the ROM.

As mentioned above, the cut-off frequency for the USABC input current is chosen as 0.4 Hz. For the ROMs generated by the Legendre polynomials, Chebyshev polynomials of the first

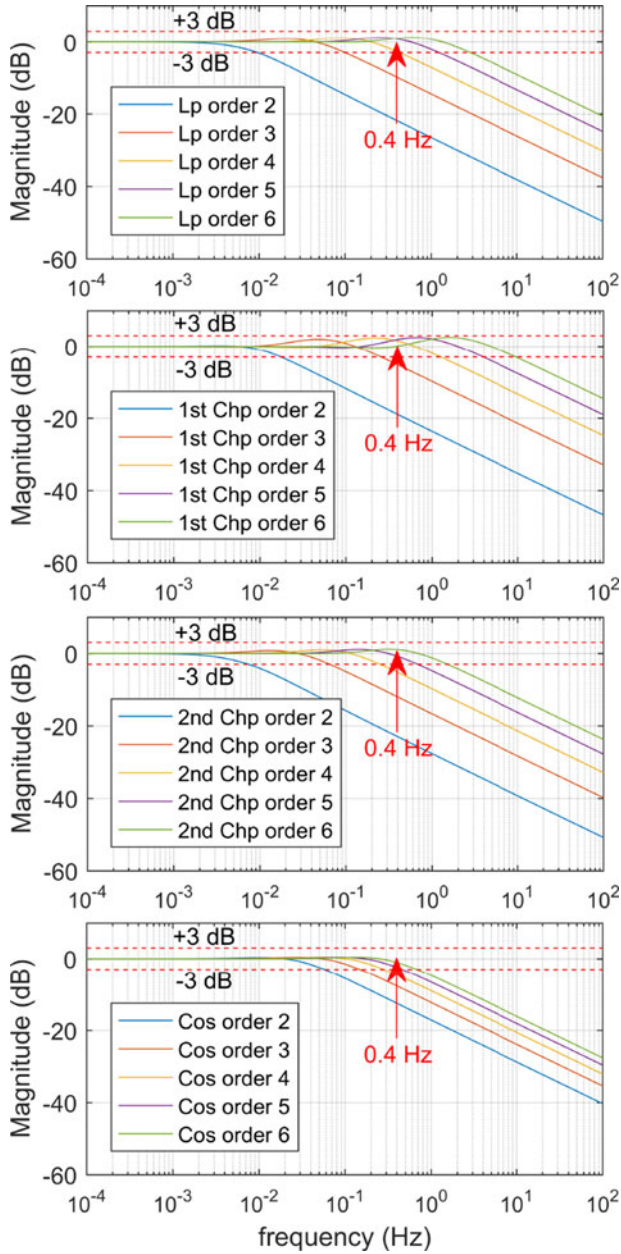


Fig. 6. Magnitude error of frequency response of ROMs using different basis functions.

kind, Chebyshev polynomials of the second kind and cosine functions, the minimum model orders that fall within the ± 3 dB frequency error bounds are the fourth order, fourth order, fifth order and fifth order, respectively, as shown in Fig. 6.

2) *Time Domain Analysis*: In time domain, the accuracy of the ROMs are evaluated using the Root-Mean-Square-Errors (RMSEs) of the surface concentration by comparing the ROMs with FDM. For instance, Fig. 7 shows surface concentration obtained by the resulting ROMs using the USABC input current profile described in Fig. 5. The RMSEs obtained for the ROMs of each class of basis functions and model order are summarized in Table II. The time domain results are consistent with the frequency-domain analysis. For in-

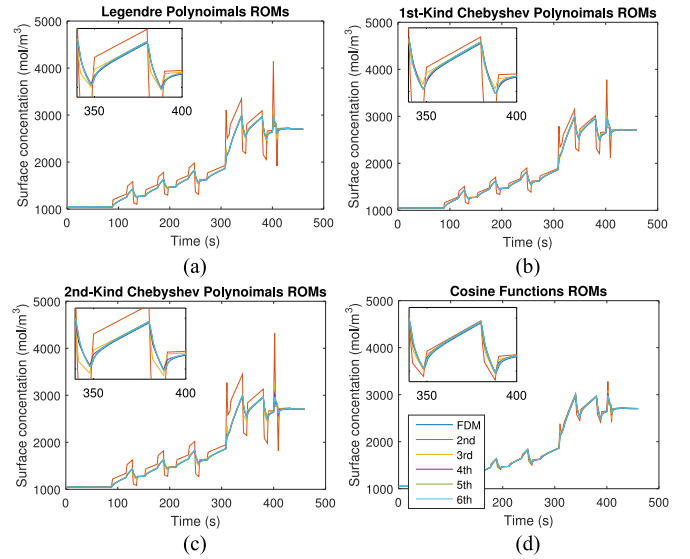


Fig. 7. Surface concentration obtained by generated ROMs.

TABLE II
SURFACE CONCENTRATION RMSEs OBTAINED BY ROMs
COMPARED WITH FDM (MOL/M³)

	Order of Truncation				
	2nd	3rd	4th	5th	6th
LP	185.1	29.7	9.5	7.6	7.5
ChP1	120.6	16.8	8.4	7.8	7.6
ChP2	218.8	42.5	13.5	8.0	7.5
Cos	46.1	20.8	12.7	9.6	8.4

stance, the surface concentration predicted by the ROM using the second-order cosine functions is more accurate than the predictions obtained using other basis functions, since the frequency response of the model approximates with the analytical solution with smaller error, as shown in Fig. 6. In addition, the accuracy of the ROM generated by the fourth-order, Chebyshev polynomials of the first kind is comparable to the accuracy of the one obtained by the sixth-order cosine functions. Nevertheless, only marginal difference in the RMSEs can be observed for the high-order ROMs obtained by different basis functions.

In summary, the selection of the basis functions and model order can be determined by conducting an error analysis either in the frequency domain or in the time domain. When the analytical solution of the PDE model is available, the frequency response of the ROMs can be compared with that of the analytical solution. By examining the comparison results at the cut-off frequency given by the input based on the pre-selected error bounds, the basis functions and model order can be determined. On the other hand, numerical solution can be calculated as the benchmark in the time domain if analytical solution is not available. RMSEs can be obtained by comparing the ROMs with the numerical solution. Therefore, basis function and model order can be selected using a pre-defined threshold on RMSE.

The procedure is then applied to the electrolyte diffusion phase. It has been shown that polynomial-based basis functions

TABLE III
SUMMARY OF THE PARAMETERS FOR THE ROM [21], [38], [39]

Symbol	Parameter	Positive electrode		Separator		Negative electrode		Units
		NMC	LFP	NMC	LFP	NMC	LFP	
L_k	Region thickness	75	80	20	20	50	43	μm
R_k	Particle radius	6.5	0.05			11	9.2	μm
$D_{s,k}$	Solid phase diffusion coefficient	1.1e-14	1.5e-18			2.5e-14	1.12e-14	$\text{m}^2 \text{s}^{-1}$
$D_{e,k}$	Liquid phase diffusion coefficient	2.0e-10	1.3e-10	2.0e-10	1.3e-10	2.0e-10	1.3e-10	$\text{m}^2 \text{s}^{-1}$
$\varepsilon_{e,k}$	Volume fraction	0.4	0.3	0.54	0.55	0.34	0.32	-
$brugg_k$	Bruggman coefficient	2.8	2	2.8	2	2.8	2	-
K_k	Kinetic rate constant	5.8e-11	2.8e-13			5.6e-11	8.8e-11	$\text{m}^{2.5} \text{mol}^{-0.5} \text{s}^{-1}$
$\varepsilon_{f,k}$	Filler volume fraction	0.2	0.2			0.06	0.05	-
$soc_{k,0}$	Initial lithiation	0.45	0.03			0.85	0.85	-
$c_{s,max,k}$	Saturation concentration	49000	22846			31423	31423	mol m^{-3}
$c_{e,0}$	Initial electrolyte concentration	1000	1000			1000	1000	mol m^{-3}
t_0^+	Transference number			0.36	0.36			-
β	activity coefficient			1.75	1.75			-
A	Current collector area	0.25	0.27			0.25	0.27	m^2

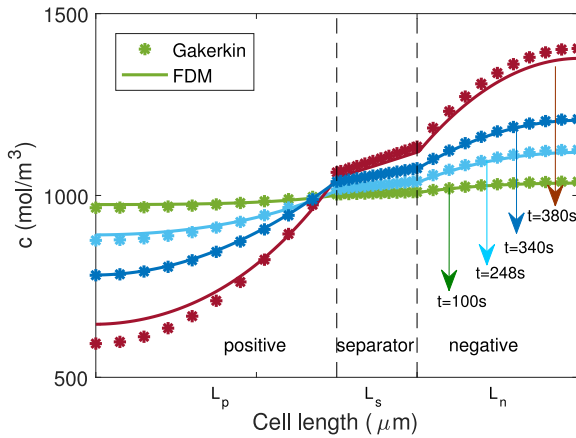


Fig. 8. Comparison of electrolyte concentration distribution obtained by the Galerkin projection method and FDM at different time points.

offer generally accurate results to approximate the diffusion PDEs and boundary conditions in this study [14], [24]. Under these circumstances, the choice of the order of the basis function should be made by evaluating the trade-off between frequency range of accuracy and computation time (which depends on the number of states of the ROM). More importantly, since the proposed model is designed for control and estimation applications, with a minor loss of accuracy, a ROM with fewer number of states is always desirable for observer design. In light of this, a third-order Legendre polynomials are chosen to approximate the liquid PDE in this study. The electrolyte concentration distribution obtained by the Galerkin projection method using the third-order Legendre polynomials is compared with FDM [37] in Fig. 8 at different time points. It is shown that only marginal differences in the concentration at the boundaries can be observed.

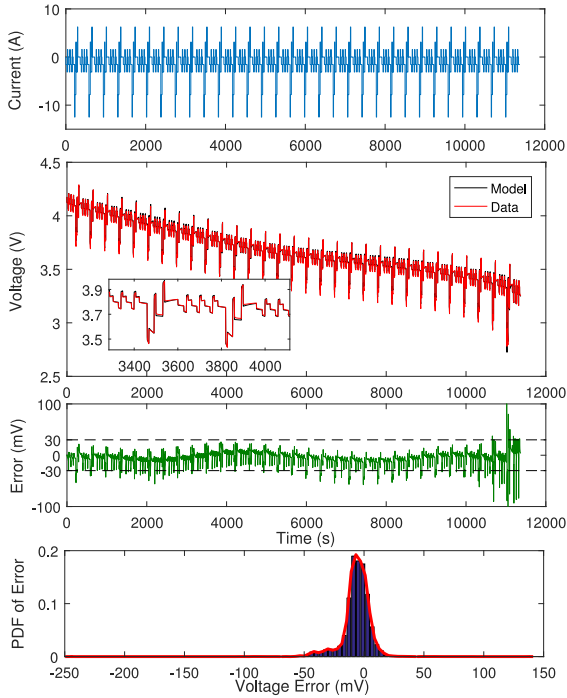
IV. VALIDATION ON CELL VOLTAGE AND DISCUSSION

Leveraging the above results, a complete reduced-order electrochemical battery model is developed by incorporating the

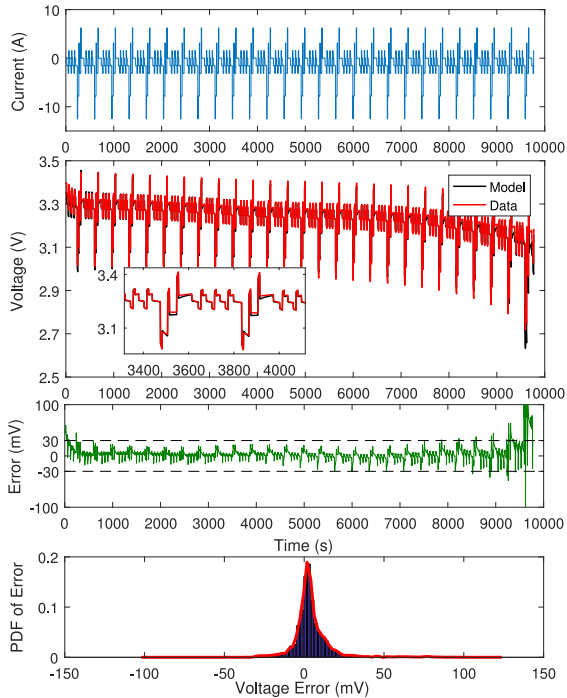
reduced-order diffusion dynamics models for the electrodes and electrolyte. While this work focused on applying the Galerkin method to the solid phase and liquid phase PDEs, Legendre polynomials are chosen here as basis functions only for illustration purposes. Particularly, based on the discussion in Section III-C, a fourth order of truncation is selected to approximate the solid diffusion PDEs and a third order is chosen for the liquid PDE.

In order to validate the resulting ROM, two battery cells with different chemistries, namely a lithium nickel manganese cobalt oxide (NMC) cell with 5.0 Ah and a lithium iron phosphate oxide (LFP) cell with 4.7 Ah, were used in this study. The cells were both cycled under different conditions, including a United States Advanced Battery Consortium (USABC) PHEV dynamic charge depleting duty cycle and a Federal Urban Driving Schedule (FUDS) duty cycle. The ambient temperature was controlled by a Testsky Instrument GDW100 environmental chamber at a constant temperature of 25 °C and current cycles were applied with an Arbin Instrument BT-2000 tester. The cell terminal voltage, current, and temperature were recorded using a sample frequency of 10 Hz. Simulations are run with MATLAB on a 2.30 GHz Intel Core i5 processor with 8 GB of RAM, using a time step $\Delta t = 1$ s.

All the electrochemical parameters used in the ROM for the two batteries are summarized in Table III. The expressions for the OCP curves with respect to state of charge can be found in Appendix. It is worth mentioning that some of the electrochemical parameters used in this work, such as the diffusion coefficients and rate constants, can be found in literature [21], [38], [39] and are tuned when necessary. There are also some parameters which are directly related to the capacity and/or voltage range of a specific cell. For example, to calibrate the electrode initial lithiations ($soc_{p,0}$, $soc_{n,0}$), typically one could start with $0.80 < soc_{p,0} < 0.9$ and adjust the $soc_{n,0}$ to match the cell voltage at 100% SOC, then work from there. For NMC battery cells, the initial lithiation $soc_{p,0}$ is usually chosen around 0.5 to match the upper voltage limit [32]. Besides, the values of the volume fraction ε_k are convoluted with the



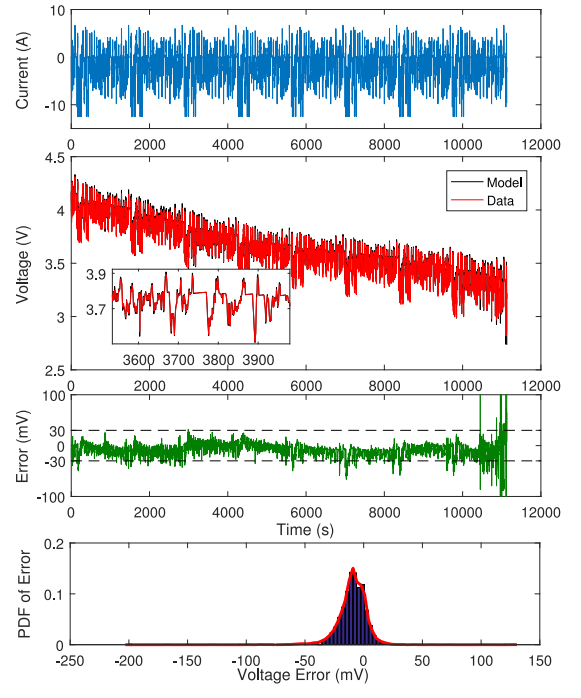
(a)



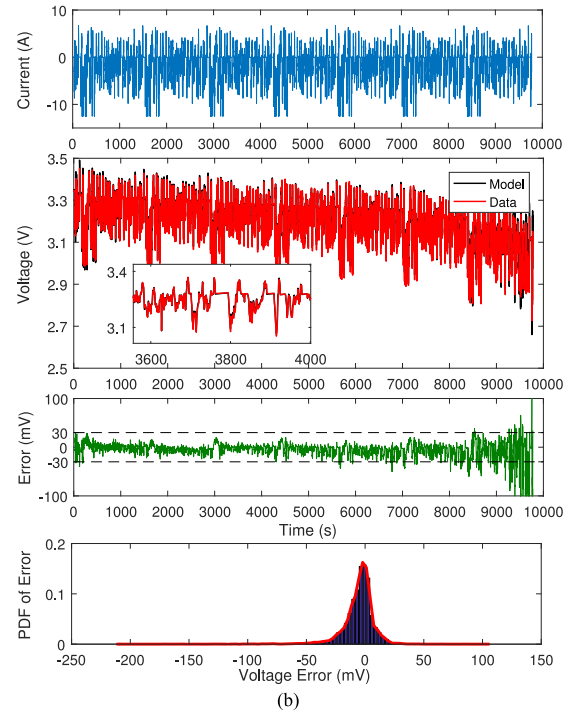
(b)

Fig. 9. Comparison of model predictions with experimental data for USABC charge depleting duty cycle. (a) NMC. (b) LFP.

electrode thickness and projected area of the unwrapped jelly roll. It is helpful if one can disassemble the cell and directly measure the coating thickness. Without that, a negative thickness can be assumed around 50–60 μm , and a positive around 60–80 μm . This should result in ε_k values around 0.5, which further assuming around 10% binder/carbon coating (inactive



(a)



(b)

Fig. 10. Comparison of model predictions with experimental data for FUDS duty cycle. (a) NMC. (b) LFP.

materials) means electrode porosity is around 0.4. As a final check of the values of $c_{s,\max,k}$ and ε_k , one can use the capacity $Q_n = \varepsilon_n * L_n * c_{n,\max} * (soc_{n,0} - soc_{n,f})$ or a similar expression for the positive electrode, and Q_n/Q_p should be close to 1.

Fig. 9 compares the voltage predicted by the ROM with experimental data for the USABC charge depleting duty cycle. As

TABLE IV
SUMMARY OF SIMULATION TIME

	Simulation Time (s)	
	USABC CD	FUDS
NMC	1.25	1.25
LFP	1.23	1.23

shown in Fig. 9, the ROM agrees very well with experimental data, with the RMSE in the voltage prediction being only 13.0 mV and 13.5 mV for NMC and LFP, respectively. The voltage prediction error is limited within a narrow error bound, i.e., less than ± 30 mV during most of the time in the driving cycle. The Probability Distribution Function (PDF) of the voltage error in Fig. 9 also demonstrates that the prediction error mainly distributes between 30 mV and 30 mV. To achieve the level of agreement shown in the figure, accurate predictions of the lithium concentration in both the electrodes and electrolyte are essential, based on which OCPs and electrolyte potential are calculated. To this extent, the comparison results also indicate that the orders of truncation selected for the solid and liquid phases are sufficient to accurately approximate the diffusion PDEs through the Galerkin projection method.

Nevertheless, it is worth noting that for both the two cells, the errors between ROM and experimental data increases during the latter stages of the profile, where cell SOC is low. One possible reason is that the diffusion coefficients of the ROM in the liquid and solid do not vary with concentration, and therefore, the local concentrations at either end of the cell (in the electrodes or the electrolyte) at low SOC could be much different than the nominal values, which in turn would lead to greater potential variation if concentration-dependent diffusion coefficients were used.

Experimental data obtained by the FUDS duty cycle are then used to further validate the ROM at different input current conditions. Again, the voltage predicted by the ROM agrees very well with experimental data, as shown in Fig. 10. The RMSE is 15.5 mV for the NMC cell, and 15.3 mV for the LFP cell. Both the error curve and the error PDF show that the prediction error mainly distributes within the range of ± 30 mV.

More importantly, the computational complexity of the electrochemical model is significantly reduced. A summary of simulation time for the four models is listed in Table IV. The computation time for the models obtained with the four MOR methods is thousands of times faster than real time. With a high level of accuracy as well as computational efficiency, the proposed Galerkin projection method will be suitable for real-time simulation, control, and estimation applications.

V. CONCLUSION

In this paper, an analytical MOR technique based upon the Galerkin projection method has been introduced systematically for electrochemical modeling of lithium-ion batteries. This approach has the advantage of greatly reducing the number of diffusion states while retaining all physically meaningful vari-

ables. Discussions on the selection of basis functions and target accuracy have been presented. The order truncation is then determined by analysis in the frequency and time domains.

The resulting ROM is then validated against the experimental data gathered from NMC and LFP batteries during USABC charge depleting and FUDS duty cycles. Comparison results show that the ROM agrees very well with experimental data at all testing conditions, with a maximum RMSE of 15.5 mV. More importantly, the computational complexity of the ESPM is significantly reduced since all the system matrices have been calculated analytically in the pre-processing phase. The ROM can be simulated thousands of times faster than the real time, making it suitable for battery state/parameter estimation, aging analysis and fault diagnosis.

APPENDIX

EXPRESSIONS OF OCPs FOR NMC AND LFP BATTERIES

NMC [39]:

$$\begin{aligned}
 U_p = & 3.72 + 0.026 \ln \frac{1 - \theta_p}{\theta_p} + 0.012(1 - \theta_p) \\
 & - 3.085(1 - \theta_p)^2 + 102.933(1 - \theta_p)^3 \\
 & - 845.20(1 - \theta_p)^4 + 3290.033(1 - \theta_p)^5 \\
 & - 6576.953(1 - \theta_p)^6 + 6567.291(1 - \theta_p)^7 \\
 & - 2605.076(1 - \theta_p)^8 - 5e^{-6} \exp\left(\frac{1}{1.08 - \theta_p}\right) \quad (48)
 \end{aligned}$$

$$U_n = 0.6379 + 0.5416e^{-305.531\theta_n} \quad (49)$$

$$\begin{aligned}
 & + 0.044 \tanh\left(-\frac{\theta_n - 0.196}{0.109}\right) - 0.1978 \tanh\left(\frac{\theta_n - 1.057}{0.085}\right) \\
 & - 0.6875 \tanh\left(\frac{\theta_n + 0.012}{0.053}\right) - 0.0175 \tanh\left(\frac{\theta_n - 0.569}{0.086}\right)
 \end{aligned}$$

LFP [21]:

$$\begin{aligned}
 U_p = & 3.43 - 0.8428e^{-80.2493(1-\theta_p)^{1.3198}} \\
 & - 3.2474 \cdot 10^{-6} e^{20.2645(1-\theta_p)^{3.8003}} \\
 & + 3.2482 \cdot 10^{-6} e^{20.2646(1-\theta_p)^{3.7995}} \quad (50)
 \end{aligned}$$

$$\begin{aligned}
 U_n = & 0.6379 + 0.5416e^{-305.531\theta_n} \\
 & + 0.044 \tanh\left(-\frac{\theta_n - 0.196}{0.109}\right) - 0.1978 \tanh\left(\frac{\theta_n - 1.057}{0.085}\right) \\
 & - 0.6875 \tanh\left(\frac{\theta_n + 0.012}{0.053}\right) - 0.0175 \tanh\left(\frac{\theta_n - 0.569}{0.086}\right) \quad (51)
 \end{aligned}$$

where

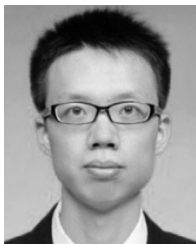
$$\begin{aligned}
 \theta_p &= \frac{C_{s,surf,p}}{C_{s,max,p}} \\
 \theta_n &= \frac{C_{s,surf,n}}{C_{s,max,n}}
 \end{aligned}$$

REFERENCES

- [1] A. Khaligh and Z. Li, "Battery, ultracapacitor, fuel cell, and hybrid energy storage systems for electric, hybrid electric, fuel cell, and plug-in hybrid electric vehicles: State of the art," *IEEE Trans. Veh. Technol.*, vol. 59, no. 6, pp. 2806–2814, Jul. 2010.
- [2] J. Vetter *et al.*, "Ageing mechanisms in lithium-ion batteries," *J. Power Sources*, vol. 147, no. 1, pp. 269–281, 2005.
- [3] M. Broussely, S. Herreyre, P. Biensan, P. Kaszlejna, K. Nechev, and R. Staniewicz, "Aging mechanism in Li ion cells and calendar life predictions," *J. Power Sources*, vol. 97, pp. 13–21, 2001.
- [4] L. Wang, E. G. Collins, and H. Li, "Optimal design and real-time control for energy management in electric vehicles," *IEEE Trans. Veh. Technol.*, vol. 60, no. 4, pp. 1419–1429, May 2011.
- [5] M. A. Roscher, J. Assfalg, and O. S. Bohlen, "Detection of utilizable capacity deterioration in battery systems," *IEEE Trans. Veh. Technol.*, vol. 60, no. 1, pp. 98–103, Jan. 2011.
- [6] H. He, R. Xiong, X. Zhang, F. Sun, and J. Fan, "State-of-charge estimation of the lithium-ion battery using an adaptive extended Kalman filter based on an improved Thevenin model," *IEEE Trans. Veh. Technol.*, vol. 60, no. 4, pp. 1461–1469, May 2011.
- [7] G. L. Plett, "Extended Kalman filtering for battery management systems of LiPB-based HEV battery packs: Part 3. State and parameter estimation," *J. Power Sources*, vol. 134, no. 2, pp. 277–292, 2004.
- [8] K. W. E. Cheng, B. Divakar, H. Wu, K. Ding, and H. F. Ho, "Battery-management system (BMS) and SOC development for electrical vehicles," *IEEE Trans. Veh. Technol.*, vol. 60, no. 1, pp. 76–88, Jan. 2011.
- [9] A. Lievre, A. Sari, P. Venet, A. Hijazi, M. Ouattara-Brigaude, and S. Pelissier, "Practical online estimation of lithium-ion battery apparent series resistance for mild hybrid vehicles," *IEEE Trans. Veh. Technol.*, vol. 65, no. 6, pp. 4505–4511, Jun. 2016.
- [10] J. Xu, C. C. Mi, B. Cao, J. Deng, Z. Chen, and S. Li, "The state of charge estimation of lithium-ion batteries based on a proportional-integral observer," *IEEE Trans. Veh. Technol.*, vol. 63, no. 4, pp. 1614–1621, May 2014.
- [11] Z. Chen, Y. Fu, and C. C. Mi, "State of charge estimation of lithium-ion batteries in electric drive vehicles using extended Kalman filtering," *IEEE Trans. Veh. Technol.*, vol. 62, no. 3, pp. 1020–1030, Mar. 2013.
- [12] J. Jagemont, L. Boulon, P. Venet, Y. Dubé, and A. Sari, "Lithium-ion battery aging experiments at subzero temperatures and model development for capacity fade estimation," *IEEE Trans. Veh. Technol.*, vol. 65, no. 6, pp. 4328–4343, Jun. 2016.
- [13] Y. Xiao, C. Lin, and B. Fahimi, "Online state of charge estimation in electrochemical batteries: Application of pattern recognition techniques," in *Proc. 2013 28th Annu. IEEE Appl. Power Electron. Conf. Expo.*, 2013, pp. 2474–2478.
- [14] R. Klein, N. A. Chaturvedi, J. Christensen, J. Ahmed, R. Findeisen, and A. Kojic, "Electrochemical model based observer design for a lithium-ion battery," *IEEE Trans. Control Syst. Technol.*, vol. 21, no. 2, pp. 289–301, Mar. 2013.
- [15] A. Bartlett, J. Marcicki, S. Onori, G. Rizzoni, X. G. Yang, and T. Miller, "Electrochemical model-based state of charge and capacity estimation for a composite electrode lithium-ion battery," *IEEE Trans. Control Syst. Technol.*, vol. 24, no. 2, pp. 384–399, Mar. 2016.
- [16] S. J. Moura, F. B. Argomedeo, R. Klein, A. Mirtabatabaei, and M. Krstic, "Battery state estimation for a single particle model with electrolyte dynamics," *IEEE Trans. Control Syst. Technol.*, vol. 25, no. 2, pp. 453–468, Mar. 2017.
- [17] Y. Xiao, "Model-based virtual thermal sensors for lithium-ion battery in EV applications," *IEEE Trans. Ind. Electron.*, vol. 62, no. 5, pp. 3112–3122, May 2015.
- [18] J. Liu, G. Li, and H. K. Fathy, "A computationally efficient approach for optimizing lithium-ion battery charging," *J. Dyn. Syst. Meas. Control*, vol. 138, no. 2, 2016, Art. no. 021009.
- [19] M. Doyle, T. F. Fuller, and J. Newman, "Modeling of galvanostatic charge and discharge of the lithium/polymer/insertion cell," *J. Electrochem. Soc.*, vol. 140, no. 6, pp. 1526–1533, 1993.
- [20] B. S. Haran, B. N. Popov, and R. E. White, "Theoretical analysis of metal hydride electrodes studies on equilibrium potential and exchange current density," *J. Electrochem. Soc.*, vol. 145, no. 12, pp. 4082–4090, 1998.
- [21] E. Prada, D. Di Domenico, Y. Creff, J. Bernard, V. Sauvant-Moynot, and F. Huet, "Simplified electrochemical and thermal model of LiFePO₄-graphite li-ion batteries for fast charge applications," *J. Electrochem. Soc.*, vol. 159, no. 9, pp. A1508–A1519, 2012.
- [22] J. Marcicki, M. Canova, A. T. Conlisk, and G. Rizzoni, "Design and parametrization analysis of a reduced-order electrochemical model of graphite/LiFePO₄ cells for SOC/SOH estimation," *J. Power Sources*, vol. 237, pp. 310–324, 2013.
- [23] C. D. Rahn and C.-Y. Wang, *Battery Systems Engineering*. Hoboken, NJ, USA: Wiley, 2013.
- [24] V. R. Subramanian, V. D. Diwakar, and D. Tapriyal, "Efficient macro-micro scale coupled modeling of batteries," *J. Electrochem. Soc.*, vol. 152, no. 10, pp. A2002–A2008, 2005.
- [25] J. C. Forman, S. Bashash, J. L. Stein, and H. K. Fathy, "Reduction of an electrochemistry-based li-ion battery model via quasi-linearization and padé approximation," *J. Electrochem. Soc.*, vol. 158, no. 2, pp. A93–A101, 2011.
- [26] K. A. Smith, C. D. Rahn, and C.-Y. Wang, "Model order reduction of 1D diffusion systems via residue grouping," *J. Dyn. Syst. Meas. Control*, vol. 130, no. 1, 2008, Art. no. 011012.
- [27] G. Fan, K. Pan, and M. Canova, "A comparison of model order reduction techniques for electrochemical characterization of lithium-ion batteries," in *Proc. 54th IEEE Conf. Decis. Control*, Osaka, Japan, 2015, pp. 3922–3931.
- [28] L. Cai and R. E. White, "Reduction of model order based on proper orthogonal decomposition for lithium-ion battery simulations," *J. Electrochem. Soc.*, vol. 156, no. 3, pp. A154–A161, 2009.
- [29] T.-S. Dao, C. P. Vyasarayani, and J. McPhee, "Simplification and order reduction of lithium-ion battery model based on porous-electrode theory," *J. Power Sources*, vol. 198, pp. 329–337, 2012.
- [30] M. A. Kehs, M. D. Beeney, and H. K. Fathy, "Computational efficiency of solving the DFN battery model using descriptor form with Legendre polynomials and Galerkin projections," in *Proc. Amer. Control Conf.*, 2014, pp. 260–267.
- [31] G. Fan and M. Canova, "Model order reduction of electrochemical batteries using Galerkin method," in *Proc. ASME 2015 Dyn. Syst. Control Conf.*, 2015, Art. no. V001T13A006.
- [32] G. Fan, K. Pan, M. Canova, J. Marcicki, and X. G. Yang, "Modeling of li-ion cells for fast simulation of high C-rate and low temperature operations," *J. Electrochem. Soc.*, vol. 163, no. 5, pp. A666–A676, 2016.
- [33] S. Santhanagopalan, Q. Guo, P. Ramadass, and R. E. White, "Review of models for predicting the cycling performance of lithium ion batteries," *J. Power Sources*, vol. 156, no. 2, pp. 620–628, 2006.
- [34] K. K. Patel, J. M. Paulsen, and J. Desilvestro, "Numerical simulation of porous networks in relation to battery electrodes and separators," *J. Power Sources*, vol. 122, no. 2, pp. 144–152, 2003.
- [35] C. Canuto, M. Y. Hussaini, A. Quarteroni, and T. A. Zang, *Spectral Methods: Fundamentals in Single Domains*. New York, NY, USA: Springer, 2006.
- [36] C. Canuto, M. Y. Hussaini, A. M. Quarteroni, and T. A. Zang, Jr., *Spectral Methods in Fluid Dynamics*. New York, NY, USA: Springer, 2012.
- [37] G. D. Smith, *Numerical Solution of Partial Differential Equations: Finite Difference Methods*. London, U.K.: Oxford Univ. Press, 1985.
- [38] V. Srinivasan and C. Wang, "Analysis of electrochemical and thermal behavior of li-ion cells," *J. Electrochem. Soc.*, vol. 150, no. 1, pp. A98–A106, 2003.
- [39] X. Li, G. Fan, G. Rizzoni, M. Canova, C. Zhu, and G. Wei, "A simplified multi-particle model for lithium ion batteries via a predictor-corrector strategy and quasi-linearization," *Energy*, vol. 116, pp. 154–169, 2016.



Guodong Fan received the B.S. degree from Dalian Jiaotong University, Dalian, China, in 2009, the M.S. degree from Tongji University, Shanghai, China, in 2012, and the Ph.D. degree from The Ohio State University, Columbus, OH, USA, in 2016. He is currently with the Technical Center of Cummins Inc., Columbus, IN, USA. His current research focuses on modeling and characterization of energy storage systems, including multiscale, multidimensional modeling, control-oriented modeling, model order reduction, and battery aging analysis.



Xiaoyu Li received the B.S. and M.S. degrees in instrument science and technology, in 2011 and 2013, respectively, from the Harbin Institute of Technology, Harbin, China, where he is currently working toward the Ph.D. degree in instrument science and technology. He was a Visiting Scholar of electrical engineering in the Center for Automotive Research, The Ohio State University, Columbus, OH, USA. His research interests include battery modeling, parameter identification, and state of health evaluation for battery second use.



Marcello Canova received the M.S. and Ph.D. degrees in mechanical engineering from the University of Parma, Parma, Italy.

He is currently an Associate Professor of mechanical engineering and an Associate Fellow of the Center for Automotive Research, The Ohio State University, Columbus, OH, USA. He has published more than 120 articles in leading journals and refereed proceedings. His current research focuses on the area of thermal sciences and energy systems, with emphasis on modeling, optimization, and associated control problems. He received the 2016 NSF CAREER Award, the Kappa Delta Distinguished Faculty Award (2011), the SAE Vincent Bendix Automotive Electronics Engineering Award (2011), the Lumley Interdisciplinary Research Award (2012), and the SAE Ralph Teetor Educational Award (2016).